

# Population density methods for stochastic neurons with realistic synaptic kinetics: Firing rate dynamics and fast computational methods

FELIX APFALTRER,<sup>1,2</sup> CHENG LY,<sup>1</sup> & DANIEL TRANCHINA<sup>3</sup>

<sup>1</sup>*Courant Institute of Mathematical Sciences, New York University, New York, NY 10012, USA*

<sup>2</sup>*Current address: Department of Mathematics, City University of New York—BMCC, New York, NY 10007, USA*

<sup>3</sup>*Department of Biology, Courant Institute of Mathematical Sciences, Center for Neural Science, New York University, New York, NY 10003, USA*

(Received 8 September; accepted October 16, 2006)

## Abstract

An outstanding problem in computational neuroscience is how to use population density function (PDF) methods to model neural networks with realistic synaptic kinetics in a computationally efficient manner. We explore an application of two-dimensional (2-D) PDF methods to simulating electrical activity in networks of excitatory integrate-and-fire neurons.

We formulate a pair of coupled partial differential–integral equations describing the evolution of PDFs for neurons in non-refractory and refractory pools. The population firing rate is given by the total flux of probability across the threshold voltage. We use an operator-splitting method to reduce computation time. We report on speed and accuracy of PDF results and compare them to those from direct, Monte–Carlo simulations.

We compute temporal frequency response functions for the transduction from the rate of postsynaptic input to population firing rate, and examine its dependence on background synaptic input rate. The behaviors in the 1-D and 2-D cases—corresponding to instantaneous and non-instantaneous synaptic kinetics, respectively—differ markedly from those for a somewhat different transduction: from *injected current input* to population firing rate output (Brunel et al. 2001; Fourcaud & Brunel 2002).

We extend our method by adding inhibitory input, consider a 3-D to 2-D dimension reduction method, demonstrate its limitations, and suggest directions for future study.

**Keywords:** *Network models*

## Introduction

Traditional methods used by neuroscientists in detailed simulations of neural networks employ Monte–Carlo techniques to simulate the stochastic nature typical of the spiking of neurons. Random behavior stems in large part from the random arrival time of the synaptic events, their random size, and random synaptic failure. It is important to retain stochastic behavior in large networks of neurons, because unphysiological population synchrony can arise in its absence. When simulating large-scale neural networks—even

---

Correspondence: Daniel Tranchina, 251 Mercer Street, New York, NY 10012, USA. Tel: +1(212) 998-3109. Fax: +1(212)995-4121. E-mail: tranchina@cims.nyu.edu

ISSN: 0954-898X print / ISSN 1361-6536 online © 2006 Informa UK Ltd.  
DOI: 10.1080/09548980601069787

with a simple integrate-and-fire underlying model—the randomness of state variables, the large number of neurons and the vastly larger number of interconnections make the computation times enormous. Consequently, computational neuroscientists have looked for approximations that consume less computation time and memory to simulate the networks.

One alternative is the *population density* (also called *probability density*) *function* (PDF) approach, which could, in principle, turn the liability of stochastic behavior into an advantage. This method has proved to be computationally efficient and accurate under certain conditions (see below), all involving restrictive approximations and/or assumptions pertaining to network connectivity and/or synaptic kinetics.

An outstanding problem that we address here is how to incorporate realistic synaptic kinetics into the population density method (PDM) in a computationally efficient manner. Our motivation stems from the fact that synaptic kinetics play an important role in network dynamics (Treves 1993; Abbott & van Vreeswijk 1993; Brunel & Hakim 1999; Nykamp & Tranchina 2000b; Haskell et al. 2001; Wang 1999; Krukowski & Miller 2001; Whittington et al. 2000; Silberberg et al. 2004; Fourcaud & Brunel 2002). The time scale of unitary postsynaptic conductance events is not always fast compared to the resting membrane time constants; so the instantaneous synaptic kinetics approximation is poor in this situation. The excitatory postsynaptic conductance channels gated by the NMDA (*N*-methyl-*D*-aspartic acid) class of glutamate receptors have particularly slow kinetics (Edmonds et al. 1995; Fain 1999), as do the metabotropic class of synaptic receptors (both excitatory and inhibitory), which gate their channels through a second-messenger system (Fain 1999). The “fast” excitatory synaptic conductances gated by the AMPA and kainate ( $\alpha$ -amino-3-hydroxy-5-methyl-4-isoxazolepropionic acid) class of glutamate receptors are diverse, and their kinetics are not always fast compared to the resting membrane time constant (Edmonds et al. 1995; Koch 1999).

The upshot is that if one wishes to explore the promise of the PDM as a time-saving computational tool, it is important to know how far one can go with population density methods while incorporating realistic synaptic kinetics. We take a first step towards answering this question here by adding realistic kinetics in the case of excitatory synaptic input only.

In the probability density method, neurons are grouped into populations of similar neurons. The population density function (PDF) for each population represents the distribution of neurons over state-space. By the law of large numbers, the average fraction of a large population of neurons that are in a certain region of state-space will be matched closely by the probability density integrated over this region; when the integrate-and-fire model is used for the underlying single-neuron model, the population firing rate is given by the total flux of probability across the threshold voltage.

The probability density function has a long history in theoretical neuroscience (Wilbur & Rinzel 1983; Tuckwell 1988b; Kuramoto 1991; Abbott & van Vreeswijk 1993; Gerstner 1999; Knight et al. 2000; Knight et al. 1996; Omurtag et al. 2000; Knight 2000; Sirovich et al. 2000; Casti et al. 2002; Sirovich 2003; Gerstner 1995; Gerstner 1999; Brunel & Hakim 1999; Brunel 2000; Amit & Brunel 1997; Mattia & Giudice 2002; Nykamp & Tranchina 2000a; Fourcaud & Brunel 2002; Brown et al. 2004; Huertas & Smith 2006; Doiron et al. 2006). Knight et al. (1996) introduced an application of the probability density function method as a time-saving computational device. Most applications of the PDM have involved underlying neurons with a one-dimensional state space. However, there have been a number of recent applications of the PDM to systems with a 2-D state space (Casti et al. 2002; Huertas & Smith 2006; Brunel et al. 2001; Fourcaud & Brunel 2002; Moreno-Bote & Parga 2004, 2005; Câteau & Reyes 2006).

If the synaptic kinetics and the membrane time constant are not on disparate time scales then the dimension of the PDF increases. For example, in the case of excitatory synaptic input only, one dimension is added for first-order synaptic kinetics, where the unitary event is a single exponential; the state space consists of two variables: voltage and excitatory conductance. Two dimensions are added for second-order kinetics, where the unitary event is a difference of exponentials. Similarly, if we add inhibition the dimension of the PDF augments accordingly. The numerical computation time for the population density method increases with each added dimension of the state space.

An unavoidable consequence of the addition of a second dimension to the state space is a loss of efficiency. We believe that accurate dimension reduction methods will need to be developed in order to make population density methods practical for realistic networks with both excitatory and inhibitory neurons. The dimension reduction methods developed so far are problematic in various ways (see Summary and Discussion).

Here, instead of focusing on dimension reduction methods, we work with a two-dimensional (2-D state space) density function. We develop numerical methods involving *operator-splitting* that prove to be efficient and accurate for simulating electrical activity in networks of excitatory neurons, and we consider two other methods as well. The methods we present here have recently been applied to the analysis and testing of the dimension reduction by moment closure method of Cai and coworkers (Cai et al. 2004, 2006). This method seemed to be so successful that it would obviate the work we present here. However, this method was recently shown to give ill posed problems for most parameters of physiological interest (Ly & Tranchina 2006), in the sense that no solutions of any kind exist for the moment closure equations. We hope that our methods will provide a benchmark for testing the speed and accuracy of future dimension reduction methods, which could, in principle, be much faster than solving the original PDF equations.

### The integrate-and-fire (I&F) neuron

In the the *integrate-and-fire* (or *Lapique*, see Tuckwell (1988a)) point neuron model, the neuron is collapsed into a single isopotential compartment, and the fast dynamics of the voltage when an action potential is generated are collapsed into one instantaneous event. In spite of the loss of detail about the shape of the action potential, this model is still a good model to simulate the firing of cortical neurons and an excellent choice for working with neural networks because it is low dimensional, and hence, faster to compute. Furthermore, Rauch et al. (2003) showed that “neocortical pyramidal cells respond as integrate-and-fire neurons to in vivo-like currents.” The input-output curves for real pyramidal cells and I&F model neurons match well (Rauch et al. 2003), but the dynamics of the firing rates may be different.

The evolution equation for the membrane potential  $V(t)$  for an integrate-and-fire neuron when there are excitatory and inhibitory synapses is given by the random differential equation (RDE):

$$c \frac{dV}{dt} + g_r(V - \mathcal{E}_r) + \hat{G}_e(t)(V - \mathcal{E}_e) + \hat{G}_i(t)(V - \mathcal{E}_i) = 0 \quad (1)$$

where  $c$  is the membrane capacitance,  $g_r$  is the resting conductance,  $\mathcal{E}_r$  is the resting potential and  $\mathcal{E}_e$  and  $\mathcal{E}_i$  are the excitatory and inhibitory equilibrium potentials, respectively. The excitatory and inhibitory conductances  $\hat{G}_e(t)$  and  $\hat{G}_i(t)$  are time dependent random variables (thus in capital letters by convention) because we regard the times and magnitudes of the underlying unitary postsynaptic events as random variables. When the stochastic membrane

potential  $V(t)$ , reaches a threshold voltage  $v_{th}$ <sup>1</sup>, the neuron is said to fire an *action potential* or *spike*. A refractory time  $\tau_{ref}$  is introduced immediately after the neuron “fires”, during which the neuron cannot fire, and the voltage is reset to  $v_{reset}$  after this *refractory period* elapses. The conductance evolves as usual during the refractory period. This period corresponds to a state in which the membrane voltage has a reduced ability to fire an action potential due to the slow inactivation of sodium conductance and the continuing activation of potassium conductance (see for example (Koch 1999)). Equation 1 holds only between firing events.

After dividing Equation 1 by  $g_r$ , we obtain one which is more convenient for our purposes:

$$\tau_m \frac{dV}{dt} + (V - \mathcal{E}_r) + G_e(t)(V - \mathcal{E}_e) + G_i(t)(V - \mathcal{E}_i) = 0 \quad (2)$$

where  $G_{e/i}(t) = \frac{\hat{G}_{e/i}(t)}{g_r}$  is the normalized excitatory/inhibitory conductance and  $\tau_m = \frac{c}{g_r}$  is the membrane time constant.

### Synaptic conductances

In our treatment, the synaptic conductances will follow first order kinetics, where the rise in conductance at the arrival of a unitary synaptic event is instantaneous and the decline is exponential. Therefore, the evolution of each synaptic conductance is given by an equation of the form

$$\tau_s \frac{d}{dt} G_s(t) + G_s(t) = \sum_k A_s^k \delta(t - T_s^k), \quad (3)$$

where the subscript  $s = e$  for excitatory or  $s = i$  for inhibitory conductance;  $T_s^k$  is the random arrival time of the  $k$ th such input;  $A_s^k/\tau_s$  is the (non-dimensional) jump in conductance upon arrival of a unitary event; and  $A_s^k$  is the area under the event waveform, *i.e.*, the integral of the normalized conductance change. We take the areas under the conductance changes  $A_s^k$  to be independent identically distributed random variables (IIDRVs), while the arrival times of the postsynaptic conductance events  $T_s^k$  are governed by an inhomogeneous Poisson process. The Poisson assumption is valid in the regime where each neuron receives input from numerous presynaptic cells with conditionally independent synaptic inputs (Nykamp & Tranchina 2000a). For sake of numerical convenience, we make the assumption that  $A_s$  follows a parabolic distribution centered on its mean  $\mu_{A_s}$  and passing through the origin. Thus, it is a one parameter distribution with support only on a line segment. The variance is  $\sigma_{A_s}^2 = \mu_{A_s}^2/5$ , so the coefficient of variation is  $\frac{\sigma_{A_s}}{\mu_{A_s}} = 0.45$ . This is similar to the coefficient of variation in our previous work (Nykamp & Tranchina 2000a). The shape of the probability density function for  $A_s$  matters little for fixed mean and variance of this random variable, provide the unitary events are not unphysiologically large.

With this description, the state variables for neurons in the non-refractory state are the transmembrane voltage  $V$ , and the excitatory and inhibitory conductances  $G_e$  and  $G_i$ , respectively.

<sup>1</sup> In our model, we consider the threshold voltage to be constant in each population to keep the dimensionality low, but this is not a necessary assumption.

*Refractory state*

While neurons are in the refractory state, their synaptic conductances continue to evolve randomly (Equation 3). There is no need to follow the dynamics of the voltage of the neurons in the refractory state, because the evolution of the voltage is not defined in this state, in accordance with the integrate-and-fire model.

The state variables for the refractory neuron are the excitatory and inhibitory conductances  $-G_e, G_i$  respectively – and  $S$ , the time since entering the refractory period.

If  $T_{th}$  denotes a time when the neuron reaches the threshold voltage, then the evolution of the state variable  $s$  of the neurons in the refractory state is given by the differential equation:

$$\frac{dS}{dt} = 1, \quad (4)$$

for  $T_{th} \leq t \leq T_{th} + \tau_{ref}$  with boundary condition  $S(T_{th}) = 0$ .

**Population density method**

The assumptions underlying our application of the population density approach, and conditions under which the evolution equation for the PDF provides an exact description of population dynamics, have been previously discussed (Nykamp 2000; Nykamp & Tranchina 2000a).

First we consider the case where neurons receive excitatory input only. At the end of the paper, we add inhibition and consider a simple method of reducing the dimension of the resulting problem from 3 to 2. This simplification gives a two-dimensional state-space for non-refractory neurons and for refractory neurons, with fluxes of probability between the refractory and non-refractory pools. The state variables for non-refractory neurons are  $V$  and  $G_e$ , while the state variables for the refractory neurons are  $S$  and  $G_e$ . For now we will drop the subscript  $e$  for excitatory conductance values and will only bring it back when we deal with inhibition at the same time.

*Non-refractory probability density*

In this two-dimensional case, the interpretation of the probability density for non-refractory neurons is:

$$\rho(v, g, t) dv \cdot dg = \Pr\{V(t) \in (v, v + dv), G_e(t) \in (g, g + dg)\} \quad (5)$$

where  $\min(v_{reset}, \mathcal{E}_r) \leq v \leq v_{th}$  and  $g \geq 0$ .

Unlike in the Monte-Carlo methods, where we have to track each neuron individually, here we look only at one probability density for each population (refractory and non-refractory).

As explained in detail in previous papers (Haskell et al. 2001; Nykamp & Tranchina 2000b; Moreno-Bote & Parga 2004, 2005; Fourcaud & Brunel 2002), Equations (2) and (3) lead to the following partial differential-integral evolution equations for the non-refractory probability density

$$\frac{\partial}{\partial t} \rho(v, g, t) = -\frac{\partial}{\partial v} \mathcal{J}_v - \frac{\partial}{\partial g} \mathcal{J}_g + \delta(v - v_{reset}) \mathcal{J}_s(\tau_{ref}, g, t) \quad (6)$$

where  $\mathcal{J}_v$  and  $\mathcal{J}_g$  are the voltage and conductance components of the non-refractory probability flux vector, respectively.  $\mathcal{J}_s$  is the refractory-time component of the refractory probability

flux.  $\mathcal{J}_s(\tau_{ref}, g, t)$  corresponds to the influx of probability per unit conductance from all the neurons which are becoming non-refractory at time  $t$ , after being in the refractory state for the refractory period  $\tau_{ref}$ . The voltage of these neurons is reset to  $v_{reset}$  at time  $t$ , as the source term indicates.

The voltage component of the probability flux vector for non-refractory neurons is purely advective in the case of non-instantaneous synaptic kinetics, because the voltage does not jump upon the arrival of an elementary synaptic event:

$$\mathcal{J}_v(v, g, t) = -\frac{1}{\tau_m}[(v - \mathcal{E}_r) + g(v - \mathcal{E}_e)]\rho(v, g, t). \quad (7)$$

The conductance component of the probability flux vector has an advective component stemming from the exponential decay of conductance to zero in the absence of synaptic input, and an integral component due to the jump in conductance upon the arrival of a synaptic event. Thus

$$\mathcal{J}_g(v, g, t) = \mathcal{J}_g^{adv}(v, g, t) + \mathcal{J}_g^{int}(v, g, t), \quad (8)$$

where

$$\mathcal{J}_g^{adv}(v, g, t) = -\frac{1}{\tau_e}g\rho(v, g, t), \quad (9)$$

and

$$\mathcal{J}_g^{int}(v, g, t) = v_e(t) \int_0^g \tilde{F}_{A_e}(\tau_e(g - g'))\rho(v, g', t)dg', \quad (10)$$

where  $\tilde{F}_{A_e}(x) = \Pr(A_e > x)$  is the complementary cumulative distribution for the unitary synaptic event conductance jump  $A_e$ .

The firing rate at a specific point in time  $r(t)$  is obtained by integrating over all excitatory conductances of the voltage component of the flux across  $v_{th}$  per unit conductance, *i.e.*:

$$r(t) = \int_0^\infty \mathcal{J}_v(v_{th}, g, t) dg = \int_{g_{th}}^\infty \mathcal{J}_v(v_{th}, g, t) dg. \quad (11)$$

The last equality is due to the fact that there is a minimum conductance ( $g_{th} = \frac{\mathcal{E}_e - v_{th}}{v_{th} - \mathcal{E}_r}$ ) that a neuron must have in order to fire an action potential (see next section for an explanation, and Figure 1).

#### *Non-refractory state in the absence of synaptic input*

In the absence of synaptic events, we obtain the  $(v, g)$  phase-plane (Figure 1) using the derivative  $dg/dv = \tau_m g / \tau_e [(v - \mathcal{E}_r) + g(v - \mathcal{E}_e)]$ , which is derived from Equations 2 and 3. Analogously,  $dg/dv = (dg/dt)/(dv/dt) = \mathcal{J}_G^{adv}/\mathcal{J}_V$  can be derived from Equations 7 and 9. Only the advective fluxes  $\mathcal{J}_v$  and  $\mathcal{J}_g^{adv}$  play a role in the population density formulation in the absence of synaptic events. The conductance decays exponentially to 0, and at every time  $t$  the voltage is driven towards a conductance dependent target voltage  $\mathcal{E}_g(t) = (\mathcal{E}_r + g(t)\mathcal{E}_e)/(1 + g(t))$ . For a fixed value of conductance  $g$ , the voltage decreases when  $v > \mathcal{E}_g$  and increases when  $v < \mathcal{E}_g$ . Therefore, the line  $(\mathcal{E}_g, g)$  naturally divides the phase plane into two (see grey diagonal almost straight line in Figure 1). This line is the  $v$ -nullcline, where  $dv/dt = 0$ . At the  $v$ -nullcline, the flow is perpendicular to the  $v$  direction at  $v = \mathcal{E}_g$ , or  $g = (v - \mathcal{E}_r)/(\mathcal{E}_e - v)$ . In order to fire, the conductance must be above the nullcline (only there, the voltage increases). Therefore, the lowest conceivable conductance value that will cause a neuron to



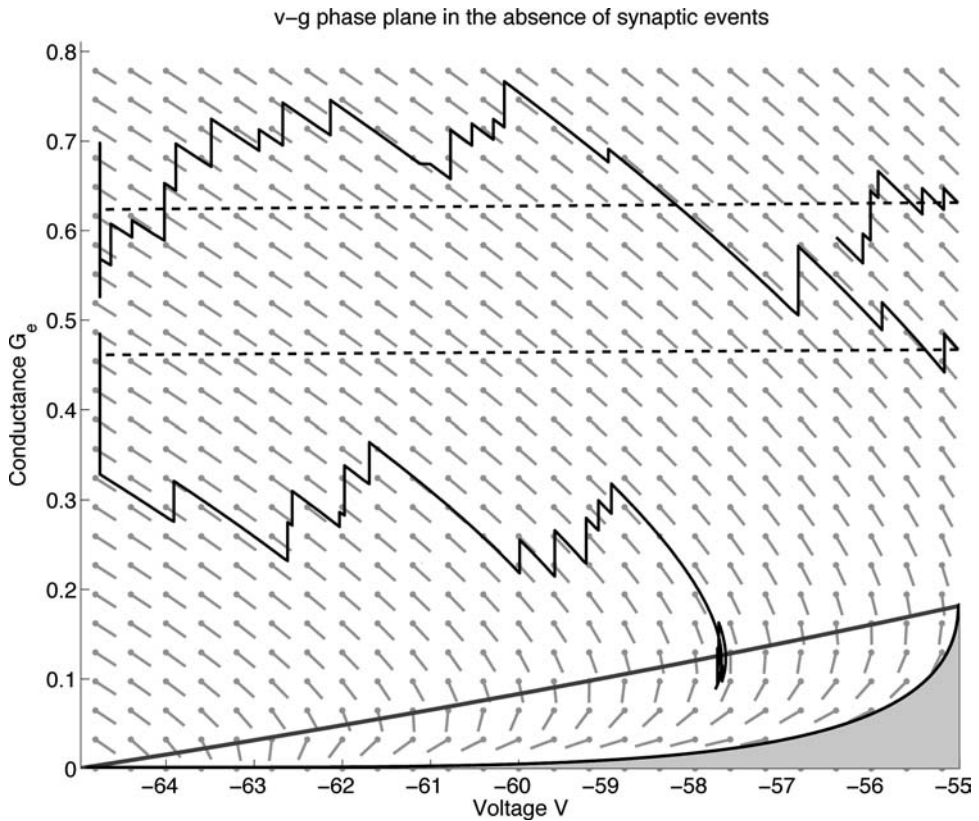


Figure 1. Non-refractory state  $v$ - $g$  phase plane and neuron's trajectory. Non-refractory state phase plane in the absence of synaptic events in grey in the background. The voltage and conductance fluxes are purely advective in the absence of events. The grey dots represent the origin of the trajectories, and the direction is given by the small lines emanating from the dots. The diagonal almost straight line is the  $v$ -nullcline (where  $dg/dv$  is singular). The black line at the bottom represents the trajectory of the  $v$  and  $g$  state variables of a neuron starting at  $(v_{th}, g_{th})$  and ending at  $(E_r, 0)$  when there are no synaptic events  $g_{th} = (v_{th} - E_r)/(\mathcal{E}_e - v_{th})$ . Since the voltage decays for all starting voltages below the  $v$ -nullcline, the region in shaded grey is never visited. We include the trajectory of one neuron starting at high voltage and conductance values (upper right region). When a synaptic event occurs, the conductance jumps vertically to a higher conductance value, but the voltage remains the same. In the absence of events, the trajectory follows the flow lines. The dotted lines indicate the voltage reset after an action potential. The conductance continues to evolve in the refractory period. For sake of illustration, this evolution is plotted at  $v_{reset} = E_r$ , and this accounts for the two vertical lines in the trajectory at  $v = E_r$ . During a time period of low synaptic input near the end of the trajectory, the neuron lingers in a state of low conductance.

fire is  $g_{th} = (v_{th} - E_r)/(\mathcal{E}_e - v_{th})$ . The voltage of any neuron below the  $v$ -nullcline will decrease over time.

The black thick line below the  $v$ -nullcline in Figure 1 represents the trajectory of the  $v$ - and  $g$ - state variables starting at  $(v_{th}, g_{th})$  and decreasing towards  $(E_r, 0)$  when there are no synaptic events. Because  $dv/dt$  is negative on this trajectory, the trajectory cannot be crossed from the left, and the region to the right is inaccessible even in the presence of synaptic input. When a synaptic event occurs, there is an upward jump in conductance while the voltage remains fixed. Therefore, the voltage and conductance will never be in the region of phase space that is shaded grey, unless the initial conditions lie in that regime. We are indebted to Bruce Knight for this insight. An example trajectory of one neuron is plotted in

solid black line, except for the dashed horizontal line showing voltage reset after the neuron crosses threshold voltage  $v_{th}$ . The vertical lines at  $v_{reset} = \mathcal{E}_r$  are included to demonstrate the evolution of the conductance while the neuron is in the refractory state.

### *Refractory probability density*

The refractory probability density function  $\sigma(s, g, t)$  has a similar but somewhat simpler partial differential-integral equation:

$$\frac{\partial}{\partial t} \sigma(s, g, t) = -\frac{\partial}{\partial s} \mathcal{J}_s(s, g, t) - \frac{\partial}{\partial g} \mathcal{J}_{g,ref}(s, g, t) \quad (12)$$

where  $s$  is the time in the refractory state. The refractory-time flux is given by

$$\mathcal{J}_s = 1 \cdot \sigma(s, g, t), \quad (13)$$

and the refractory conductance flux is given by

$$\mathcal{J}_{g,ref} = \mathcal{J}_{g,ref}^{adv} + \mathcal{J}_{g,ref}^{int}. \quad (14)$$

Here, the refractory conductance flux  $\mathcal{J}_{g,ref}$  has been subdivided like its non-refractory counterpart, into an advection component

$$\mathcal{J}_{g,ref}^{adv} = -\frac{1}{\tau_e} g \sigma(s, g, t), \quad (15)$$

and an excitatory integral component

$$\mathcal{J}_{g,ref}^{int} = v_e(t) \int_0^g \tilde{F}_{A_e}(\tau_e(g-g')) \sigma(s, g', t) dg'. \quad (16)$$

The flux of probability across threshold into the refractory state gives the boundary condition:

$$\mathcal{J}_v(v_{th}, g, t) = \mathcal{J}_s(0, g, t). \quad (17)$$

It is worth emphasizing that  $\rho$  and  $\sigma$  are absolute rather than conditional probability densities. The conservation of probability law means that

$$\int_{\min(v_{reset}, \mathcal{E}_r)}^{v_{th}} \int_0^\infty \rho(v, g, t) dv dg + \int_0^{\tau_{ref}} \int_0^\infty \sigma(s, g', t) ds dg' = 1. \quad (18)$$

### **Single uncoupled population: PDM versus monte carlo**

In this section, we test our 2-D population density methods for a single uncoupled population with only external synaptic input at a specified rate. By the law of large numbers, we know that the Monte-Carlo (MC) simulations converge to the average firing rate as the population size approaches infinity. We measure the computation times that our simulations take and make efficiency-accuracy comparisons for the Monte-Carlo and probability density methods.

We tested our method for synaptic input rates given by arbitrary, temporally rich, random sums of sinusoidal inputs. This type of input was used previously in a number of studies to test population density methods (Nykamp & Tranchina 2000a, 2000b, Haskell et al. 2001).

Details of our operator splitting numerical method for solving the system of PDEs for the non-refractory probability density,  $\rho(v, g, t)$ , and refractory probability density  $\sigma(v, g, t)$



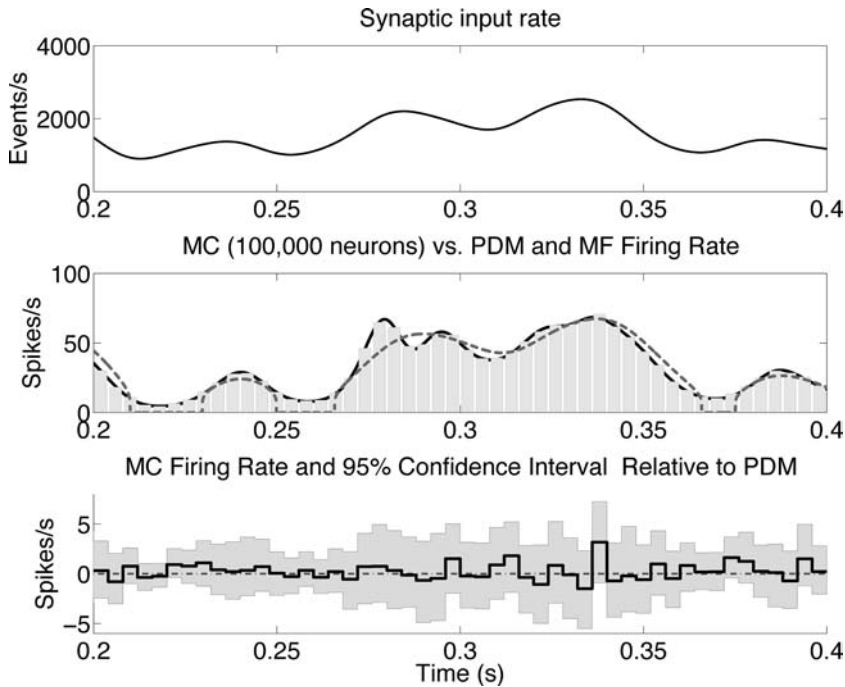


Figure 2. Single uncoupled population results: PDM vs. MC for 100,000 neurons in direct simulation. Top panel: the synaptic input rate over a 200 ms stimulus epoch. Middle panel: output firing rate of a single uncoupled population of neurons computed by the PDM (solid black line), direct Monte-Carlo (MC) simulation with a population of 100,000 individual I&F neurons (grey histogram), and fully mean-field firing rate method (dashed line). The PDM results were computed with the finest grid refinement and smallest time step; they provide the benchmark against which all errors were computed. Bottom panel: statistical comparison between PDM and MC, in which each rate is offset (shifted) by the PDM firing rate, to make the magnitude of the discrepancy clear. The bottom panel shows: the mean MC firing rate (100,000 neurons, solid black line); 95% confidence region for the MC firing rate (delimited by grey cloud); the PDM firing rate (dot-dash), which is equal to zero by definition in these shifted coordinates. The PDM firing rate was averaged over the same time bin used to compute the MC firing rate. The 95% confidence region for the MC firing rate was computed by a bootstrap method in which entire spike trains were resampled (sampling with replacement) from the stored spike trains of 100,000 I&F neurons. One thousand bootstrap firing rates were computed. The grey cloud encloses entirely those bootstrap firing rates that were in the lowest 95 percentile of Euclidean distances from the original MC firing rate. The PDM firing rate is close to the middle of the 95% confidence interval for the *true population firing rate* that the direct MC simulation estimates. For the PDM: time step  $\Delta t = \tau_e/160 = 31.25 \mu\text{s}$ ; 64 conductance and voltage grid points. Parameters:  $\tau_m = 20 \text{ ms}$ ,  $\tau_e = 5 \text{ ms}$ ,  $\tau_{ref} = 3 \text{ ms}$ ,  $\mu_A = 1.538 \times 10^{-4} \text{ s}$ , giving  $\mu_{EPSP} = 0.31 \text{ mV}$ . For the MC computations, the time step was determined by synaptic events in the event-driven simulation (Appendix D), with a maximum time step (in the absence of events) of 1 ms.

are given in Appendix A. We also present two alternatives in Appendix A: a single operator method; and a moving eigenvector basis method that allows dimension reduction.

Figure 2 shows the rate of external postsynaptic conductance events (top panel) and the output firing rate of a single uncoupled population of neurons (middle panel) computed by: the PDM (solid black line); fully mean-field firing rate method (Appendix E, dashed line); and by a direct Monte-Carlo (MC) simulation with a population consisting of 100,000 I&F neurons (grey histogram). The PDM results in this figure were computed with the finest grid refinement and smallest time step that we used in our second-order accurate method; they provide the benchmark against which all errors were computed. Good agreement, suggested in the middle panel, between PDM (solid line) and MC (grey histogram) is confirmed by

the statistical analysis illustrated in the bottom panel. The firing rate computed by the full mean-field method (middle panel, dashed line) does not capture details of the firing rate dynamics and misses low firing rates completely. The bottom panel shows the following: the mean MC firing rate (100,000 neurons, solid black line); 95% confidence region for the *true MC population firing rate* (delimited by grey cloud); and PDM firing rate (dot-dash). The interpretation of this confidence cloud is that, upon repeated construction of such confidence clouds based on independent, similarly computed MC simulations (Appendix D), the probability that the true MC population firing rate (hypothetical rate that would be computed in the limit of an infinite number of neurons) would not be entirely contained within any randomly chosen cloud would be 0.05. The PDM firing rate in the bottom panel is averaged over the same time bin used to compute the MC firing rate. To make the magnitude of the discrepancies clear, each rate is offset by the PDM firing rate. The PDM firing rate is close to the middle of the 95% confidence region for the “true” MC population firing rate that the direct MC simulation nominally estimates. It is worth keeping in mind that the MC simulation itself, as a consequence of practical considerations concerning the numerical methods, necessarily has some small error even in the limit as the number of neurons approaches infinity.

*Efficiency and accuracy: Error versus computation time for PDM and MC.* Figure 3 shows how the root-mean-square error (bootstrap estimate) depends on computation time for PDM and MC in the case of a single uncoupled population of neurons receiving excitatory synaptic input at a specified rate. Error is defined as deviation from the “converged” PDM firing rate; i.e., that computed with the finest grid refinement and the smallest time step. The

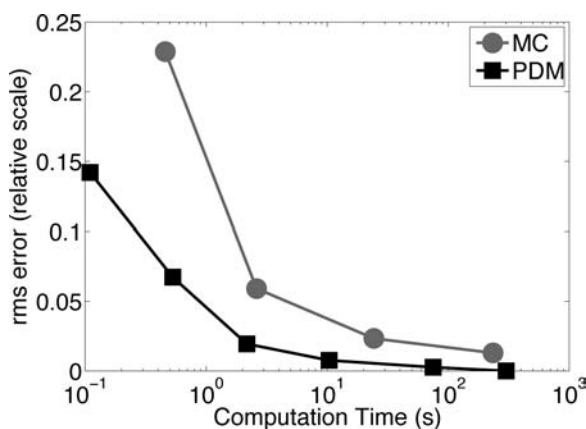


Figure 3. Accuracy as a function of computation time for PDM and MC with single uncoupled population. Fractional root-mean-square error: dependence on computation time for PDM and MC in the case of a single uncoupled population of neurons receiving excitatory synaptic input at a specified rate. Fractional root-mean-square error was computed by dividing root-mean-square error by the norm of the PDM firing rate vector, computed with the finest grid refinements and smallest time step. Mean-square error itself is equal to bias plus squared variance. For the MC, the computation time is proportional to number of neurons in the population. For the PDM, the computation time is determined by the refinement of the voltage ( $v$ ) and synaptic conductance ( $g$ ) grids as well as the time step ( $\Delta t$ ). The finer the grid, the more accurate the PDM results. The MC were obtained from runs with  $n = 100, 1,000, 10,000$ , and  $100,000$  I&F neurons. Mean square error for  $n$  MC neurons was estimated by a bootstrap method in which  $n$  spike trains were resampled (with replacement) repeatedly from a stored group of 100,000 spike trains. PDM results were obtained from various grid refinements with time steps  $\Delta t = 1, 1/2, 1/4, 1/8, 1/16$  and  $1/32$  ms, using 14, 20, 28, 40, 64 and 80 conductance and voltage bins respectively. Parameters: same as Figure 2.

root-mean-square error is measured relative to the norm of the converged PDM firing rate vector. It is worth keeping in mind that mean-square error itself is equal to variance plus squared bias. In the case of the PDM, error is entirely due to bias, while for the MC both variance and bias contribute to the error. The computation time for MC is proportional to number of neurons used to estimate the population firing rate, while for the PDM, the computation time is determined by the refinement of the voltage ( $v$ ) and synaptic conductance ( $g$ ) grids as well, as the time step ( $\Delta t$ ).

Figure 3 shows that, for a relative error 5% for both PDM and MC, the PDM is about 3 times faster than the MC; for a relative error of 2%, the PDM is about 30 times faster. The data in Figure 3 also show that the computation time required for a relative error of 2% in the PDM corresponds to a MC simulation with 600 neurons.

### PDM in neural networks

The previous results were for a single population of excitatory neurons, but we wish to apply the PDM to simulate large networks of populations. We implement this following Nykamp & Tranchina (2000a). We group the neurons into populations of similar biophysical properties which we label with the index  $k$  ( $k = 1, 2, \dots, M$ ), where  $M$  is the number of populations. For each population, we form a non-refractory and a refractory probability density function,  $\rho^k(v, g, t)$  and  $\sigma^k(s, g, t)$ , respectively. Then we define the connectivity between the populations by a population connectivity matrix  $W_{ij}$  where  $i, j = 1, 2, \dots, M$ . In a strictly corresponding Monte-Carlo simulation, each neuron in a population receives synaptic input with identical average input rate. In this case, the interpretation of  $W_{ij}$  is that every neuron in population  $j$  receives an exact fraction  $W_{ij}$  of all possible connections from neurons in population  $i$ .

This assumption can be relaxed in Monte-Carlo simulations by letting  $W_{ij}$  be the probability that a presynaptic neuron in population  $j$  receives synaptic input from any randomly selected neuron in population  $i$ . We found that this relaxation (used here) improves the agreement between the population density results and the Monte-Carlo results (averaged over random network realizations) for small population sizes. This finding is consistent with that of Nykamp & Tranchina (2000a) in the 1-dimensional case.

In the case of a single population we considered only external input, but when several populations are coupled together, the synaptic input rate into population  $j$  is determined by the external input rate into the population  $v_o^j(t)$  as well as by the synaptic input from other populations. For example, in the primary visual cortex the “internal” presynaptic input from other populations comes from the cortico-cortical connections, while the external input comes from the LGN. Therefore, the synaptic input rate into population  $j$  is given by:

$$v^j(t) = v_o^j(t) + \sum_{i=1}^M N_i W_{ij} \int_{-\infty}^t \alpha_{ij}(t-t') r_i(t') dt', \quad (19)$$

where  $N_i$  is the number of neurons in population  $i$ ,  $\alpha_{ij}(t)$  is the probability density function for the synaptic delay between presynaptic neurons in population  $i$  and neurons in population  $j$  and  $r_i(t)$  is the population firing rate of the  $i$ th population. The connectivity is stochastic so that  $N_i W_{ij}$  is the expected number of synaptic inputs from population  $i$  to each neuron in population  $j$ . Any pair of neurons in populations  $i$  and  $j$  are connected with probability  $W_{ij}$ .

If we add *synaptic failure* and let  $p$  be the probability that synaptic transmission from a presynaptic neuron fails, then we implement this failure rate in our Monte-Carlo simulations by randomly dropping a unitary postsynaptic conductance event in the postsynaptic partner

(event by event and synapse by synapse, in an independent manner) with probability  $p$ . In our probability density method on the other hand, we multiply the connections to the postsynaptic partners with the probability that a synaptic event does indeed occur ( $1 - p$ ). Therefore Equation 19 is slightly altered in our PDM to obtain

$$v^j(t) = v_o^j(t) + (1 - p) \sum_{i=1}^M N_i W_{ij} \int_{-\infty}^t \alpha_{ij}(t - t') r_i(t') dt'. \quad (20)$$

### PDM outperforms MC in neural network simulations

Figure 4 shows how computation time for PDM and MC depend on the number of interacting populations  $n$  in an excitatory neural network. In this illustration a neuron in population  $k$  receives synaptic input from a randomly chosen neuron in population  $j$  with probability 0.2, where  $j, k = 1, 2, \dots, n$ . The MC simulation consisted of one realization of this network and a single stimulus epoch (period is the same for MC and PDM). In addition, each population receives external synaptic input at a specified rate. Because these neural networks contain excitatory input only,  $\mu_{EPSP}$  (determined by  $\mu_A$ ) is scaled with the number of interacting populations, to prevent explosion of the population firing rates. This is the only fair way to examine how computation time depends on population number for purely excitatory networks.

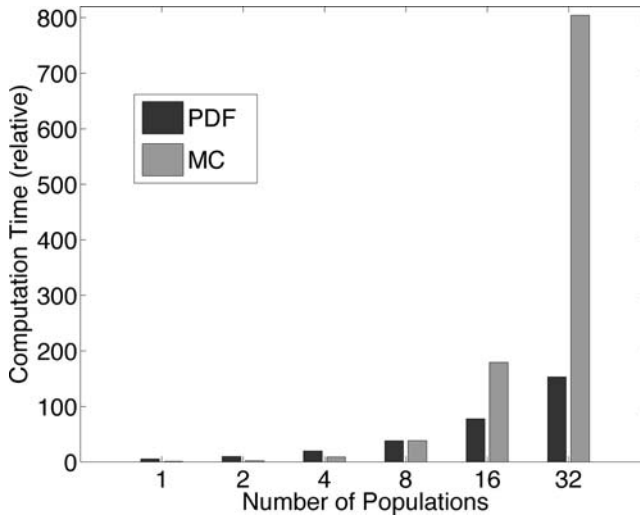


Figure 4. Computation time as a function of population size for PDM versus MC. Computation time (as measured by central processing unit, cpu, time on the computer) for PDM (black bars) and MC (grey bars) as a function of the number of interacting populations  $n$  in an excitatory neural network; relative to computation time of single population MC simulation. Connectivity as follows: a randomly chosen neuron in population  $k$  receives synaptic input from a randomly chosen neuron in population  $j$  with probability 0.2, where  $j, k = 1, 2, \dots, n$ . The MC simulations used to estimate population firing rates in each case consisted of one realization of each network of  $n$  populations and a single stimulus epoch (period is the same for MC and PDM). In addition, each population receives external synaptic input at a specified rate. Because these neural networks contain excitatory input only,  $\mu_{EPSP}$  (determined by  $\mu_A$ ) is scaled with the number of interacting populations, to prevent explosion of the population firing rates. The computation time for MC depends quadratically on the number of interacting populations,  $n$ , while for PDM it depends linearly on the number of populations. Time step  $dt = \tau_e / 10 = 0.5$  ms; 25 conductance and voltage grid points. Parameters:  $\tau_m = 20$  ms,  $\tau_e = 5$  ms,  $\tau_{ref} = 3$  ms.

Figure 4 illustrates that the computation time for MC depends quadratically on the number of interacting populations  $n$  (also on the total number of neurons), while for PDM it depends linearly on the number of populations. Consequently, once  $n$  exceeds a certain number, PDM will win out over MC.

For the simulations in Figure 4, PDM is already slightly faster than MC with only  $n = 8$  populations, despite the fact that there are only 50 neurons in each population, and that the MC firing rate was computed with only one stimulus pass.

Figure 5B shows results of one simulation giving the 2-population data point in Figure 4 above (PDM in solid black line, MC in grey histogram). Because the MC firing rate was computed on the basis of one realization of the 2 population network, the estimated population firing rates are quite rough. Panel A (Figure 5) shows the rate of external synaptic input events into populations 1 and 2, while panel C shows MC firing rates obtained from

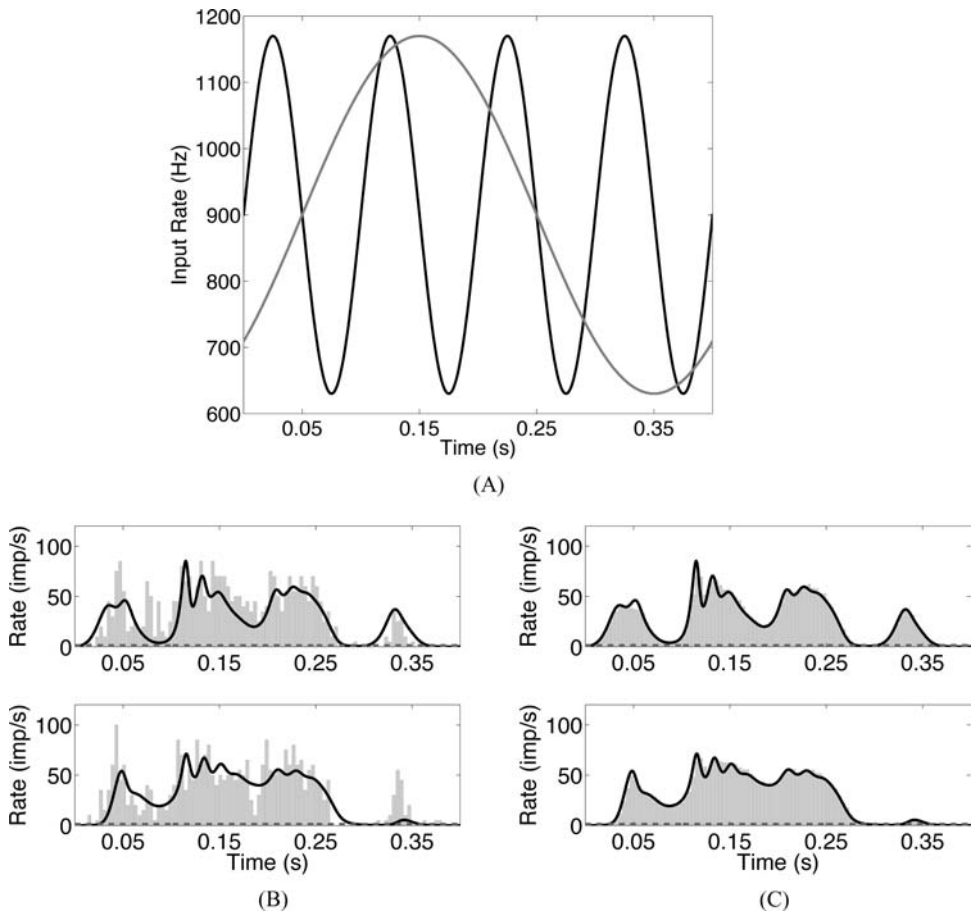


Figure 5. Monte-Carlo and PDF simulations for a two-population network in which each possible synaptic connection is made with 20% probability. Panel A shows external synaptic input into population 1 (black) and 2 (grey). Panel B shows firing rates for populations 1 and 2 (upper and lower panels, respectively) computed by: the PDM (solid line); MC simulation with 50 neurons per population, a single network realization, and a single stimulus epoch (grey histogram); and mean-field firing rate model (dashed line). Panel C is the same as panel B except that the MC firing rate was obtained by averaging over 100 network realizations. Time step  $dt = \tau_e/10 = 0.5$  ms; 25 conductance and voltage grid points. Parameters:  $\tau_m = 20$  ms,  $\tau_e = 5$  ms,  $\tau_{ref} = 3$  ms.

averaging over 100 realizations (50 neurons per population). Panel C illustrates that the PDM can capture MC firing rates when the number of neurons per population is small (50 in this case), even when the connectivity is not terribly sparse. This is consistent with the findings of Nykamp & Tranchina (2000a). The firing rate computed by the mean-field firing rate method (Appendix E) in Figures 5B and 5C (dashed line) is identically 0, because the external synaptic input rates fall below the threshold rate for a non-zero output firing rate.

In computations not shown, we found that deviations between MC and PDM for denser connectivity are not improved appreciably by a modest rate of synaptic failure, e.g., probability of successful synaptic transmission  $p = 0.8$ . This is also consistent with findings of Nykamp & Tranchina (2000a).

### Frequency response and impulse response of the population firing rate

We consider the frequency response of an uncoupled population of identical neurons receiving synaptic input at a specified rate. The transduction we are considering is the one in which the rate of unitary postsynaptic conductance events is considered as the input, and the population firing rate is regarded as the output, as in Knight (2000). This is different from the transduction considered by Fourcaud & Brunel (2002), Brunel et al. (2001), in which the input was external current injected directly into the I&F neuron. The qualitative and quantitative features of the frequency responses for the two transductions differ.

We examine the frequency response in the context of the problem in which the density  $\rho$  is discretized over both  $v$  and  $g$  for the 2-D problem (see Appendix A, Numerical methods 63), and over  $v$  for the 1-D problem as in (Nykamp & Tranchina 2000a); these two cases correspond to non-instantaneous and instantaneous synaptic kinetics, respectively. We checked to make sure that the results do not differ appreciably if the  $v$  and  $g$  grids are refined further. Thus, our results provide a close approximation to those in the limit of the continuous  $\rho(v, g, t)$  problem.

In both the 1-D and 2-D problems, the evolution equation for the discretized probability density vector (see Appendix A)  $\vec{\rho}(t)$  is governed by an equation of the form:

$$\frac{d\vec{\rho}}{dt} = Q(v_e(t))\vec{\rho}, \quad (21)$$

where  $Q(v_e(t))$  is a matrix.

To compute the frequency response, we begin by linearizing the system around a steady state. We consider an input consisting of a steady synaptic input rate  $v_0$  and a superimposed time-varying perturbation  $\epsilon v_1(t)$ , so that

$$v_e(t) = v_0 + \epsilon v_1(t), \quad (22)$$

where  $\epsilon$  is a parameter that determines the magnitude of the perturbation, and  $\epsilon v_1(t)$  is small compared to  $v_0$ .

Such an input results in a density  $\vec{\rho}(t)$  and a population firing rate response  $r(t)$ , each of which can be expressed in Taylor series in  $\epsilon$ :

$$\vec{\rho}(t) = \vec{\rho}_0 + \epsilon \vec{\rho}_1(t) + O(\epsilon^2), \quad (23)$$

and

$$r(t) = r_0 + \epsilon r_1(t) + O(\epsilon^2). \quad (24)$$

We show below that a qualitative difference in response dynamics between the 1-D and 2-D problems arises from the different nature of relevant probability fluxes in the two problems.



In the 2-D problem the firing rate is given by the advective marginal voltage flux evaluated at threshold, and it has no explicit dependence on the synaptic input rate. In the 1-D problem, the voltage flux comes from jumps in voltage upon arrival of synaptic events, and it is given by an integral term that is multiplied by the synaptic input rate.

*Frequency response and impulse response for I&F neurons with a 2-D state space, non-instantaneous synaptic kinetics*

For the 2-D problem (see Appendix A (64)),

$$r(t) = \vec{b} \cdot \vec{\rho}(t), \quad (25)$$

where  $\vec{b}$  is a constant vector.

Substituting Equations 22 and 23 into Equations 21 and 25, and collecting terms up to first order in  $\epsilon$  gives equations for the zero-order and first-order terms for probability density function and corresponding firing rate. The 0th order equations are:

$$Q(v_0) \vec{\rho}_0 = 0, \quad (26)$$

and

$$r_0 = \vec{b} \cdot \vec{\rho}_0. \quad (27)$$

The first-order (in  $\epsilon$ ) equations are:

$$\frac{d\vec{\rho}_1}{dt} = Q(v_0) \vec{\rho}_1(t) + v_1(t) \frac{dQ}{dv} \vec{\rho}_0, \quad (28)$$

and

$$r_1(t) = \vec{b} \cdot \vec{\rho}_1(t). \quad (29)$$

Note that the steady-state solution  $\vec{\rho}_0$  in Equation 26 is simply the normalized eigenvector of the matrix  $Q(v_0)$  (Knight 2000) with 0 eigen-value.<sup>2</sup>

When the time-dependent input is sinusoidal,  $v_1(t) = \Re[\mathcal{V} e^{i\omega t}]$  (we omit  $\Re$  below, as it is implied in linear systems analysis by convention), the first-order terms for density and firing rate will also be sinusoidal. Therefore,  $\vec{\rho}_1(t) = \vec{\rho} e^{i\omega t}$  and  $r_1(t) = \mathcal{R} e^{i\omega t}$ .

To solve for  $\vec{\rho}$  and  $\mathcal{R}$  we substitute our expressions for  $v_1(t)$  and  $\vec{\rho}_1(t)$  into Equations 28 and 29 to obtain:

$$\begin{aligned} (i\omega I - Q(v_0))\vec{\rho} &= \mathcal{V} \frac{dQ}{dv} \vec{\rho}_0 \\ \Rightarrow \vec{\rho} &= \mathcal{V} (i\omega I - Q(v_0))^{-1} \frac{dQ}{dv} \vec{\rho}_0, \quad \text{for } \omega \neq 0, \end{aligned} \quad (30)$$

and

$$\mathcal{R} = \vec{b} \cdot \vec{\rho}, \quad (31)$$

where  $I$  is the identity matrix. The equation for  $\vec{\rho}$  can also be written in an eigenvector expansion by using the eigenvectors of the operator  $Q(v_0)$ , as in Knight (2000):

$$\vec{\rho} = \mathcal{V} \sum_{n \neq 0} \frac{(\vec{\phi}_n^*, \frac{dQ}{dv} \vec{\rho}_0)}{i\omega - \lambda_n} \vec{\phi}_n, \quad (32)$$

<sup>2</sup> The operator  $Q(v_0)$  has one 0 eigen-value. The rest of the eigen-values all have negative real part.

where  $\vec{\phi}_n$  and  $\vec{\phi}_n^*$  are the eigenvectors of  $Q(v_0)$  and its transpose, respectively. The complex dot product is defined by:

$$\vec{w} \cdot \vec{v} \equiv (\vec{w}, \vec{v}) \equiv \sum_{j=1}^N \bar{w}_j \cdot v_j,$$

where  $\bar{w}_j$  is complex conjugation. The  $N$  eigen-vectors (indexing begins at 0) are normalized so that  $(\vec{\phi}_m, \vec{\phi}_n) = \delta_{mn}$ . We have  $\vec{\phi}_0 = \vec{\rho}_0$ , and  $0 = \lambda_0 > \Re(\lambda_1) \geq \Re(\lambda_2) \geq \dots \geq \Re(\lambda_{N-1})$ , where the real parts are all negative.

The frequency response,  $Z(\omega; v_0)$  measured at background synaptic input rate  $v_0$  and evaluated at frequency  $\omega$ , is defined by

$$\begin{aligned} Z(\omega; v_0) &= \mathcal{R}/\mathcal{V} \\ &= \vec{b} \cdot \left[ (i\omega I - Q(v_0))^{-1} \frac{dQ}{dv} \vec{\rho}_0 \right] \end{aligned} \quad (33)$$

$$\begin{aligned} &= \vec{b} \cdot \left[ \sum_{n \neq 0} \frac{(\vec{\phi}_n^*, \frac{dQ}{dv} \vec{\rho}_0)}{i\omega - \lambda_n} \vec{\phi}_n \right] \\ &= \sum_{n \neq 0} \frac{(\vec{\phi}_n^*, \frac{dQ}{dv} \vec{\rho}_0) (\vec{b}, \vec{\phi}_n)}{i\omega - \lambda_n} \end{aligned} \quad (34)$$

$Z(\omega; v_0)$  is the complex number whose modulus is the gain, and whose argument (angle in the complex plane) is the phase of the frequency response.

The corresponding impulse response function of the population firing rate,  $z(t; v_0)$ , can be thought of as the average population response to the arrival of a single unitary postsynaptic conductance event (of random magnitude), when it is superimposed on a background synaptic input rate  $v_0$ . This impulse response function is given by the inverse Fourier transform of  $Z(\omega; v_0)$ . The impulse response function can be computed analytically from Equation 34 above:

$$z(t; v_0) = \left[ \sum_{n \neq 0} \left( \vec{\phi}_n^*, \frac{dQ}{dv} \vec{\rho}_0 \right) (\vec{b}, \vec{\phi}_n) e^{\lambda_n t} \right] H(t), \quad (35)$$

where  $H(t)$  is the unit (Heaviside) step function.

For sake of comparison, we also examine the frequency response of the mean postsynaptic conductance, which drives the population firing rate. It is worth keeping in mind that the population firing rate is not completely determined by the mean postsynaptic conductance, so the relationship between the firing rate frequency response and conductance frequency responses changes with background synaptic input rate  $v_0$ . The evolution of the mean excitatory conductance is governed by the first-order linear ODE

$$\frac{d\mu_G(t)}{dt} = -\frac{1}{\tau_e} (\mu_G(t) - v_e(t) \mu_{A_e}). \quad (36)$$

Following the same strategy as above yields the frequency response  $\mathcal{M}_G(\omega)$  for the mean excitatory postsynaptic conductance,

$$\mathcal{M}_G(\omega) = \frac{\mu_{A_e}}{1 + i\omega\tau_e}. \quad (37)$$

and the corresponding impulse response function,

$$m_G(t) = \frac{\mu_{A_e}}{\tau_e} e^{-t/\tau_e} H(t). \quad (38)$$

Figure 6 shows the absolute gain in linear—log coordinates (panel A), normalized gain in log—log (Bode-plot) coordinates (panel B), and phase lag in linear-log (Bode-plot) coordinates (panel C), as functions of frequency  $f$  in Hz (where  $\omega = 2\pi f$ ) for the 2-D population firing rate frequency response,  $\mathcal{Z}(\omega; \nu_0)$ . Each graph shows a family of curves corresponding to various background synaptic input rate,  $\nu_0$ , values. It is worth keeping in mind that gain at  $\omega = 0$  is equal to the (algebraic) area under the impulse response function, i.e.,

$$\mathcal{Z}(0; \nu_0) = \int_0^\infty z(t; \nu_0) dt. \quad (39)$$

Consequently,  $\mathcal{Z}(0; \nu_0)$  is sometimes used as a measure of “overall gain”; it gives the net change in the total number of spikes that is elicited by a single synaptic event, on average,

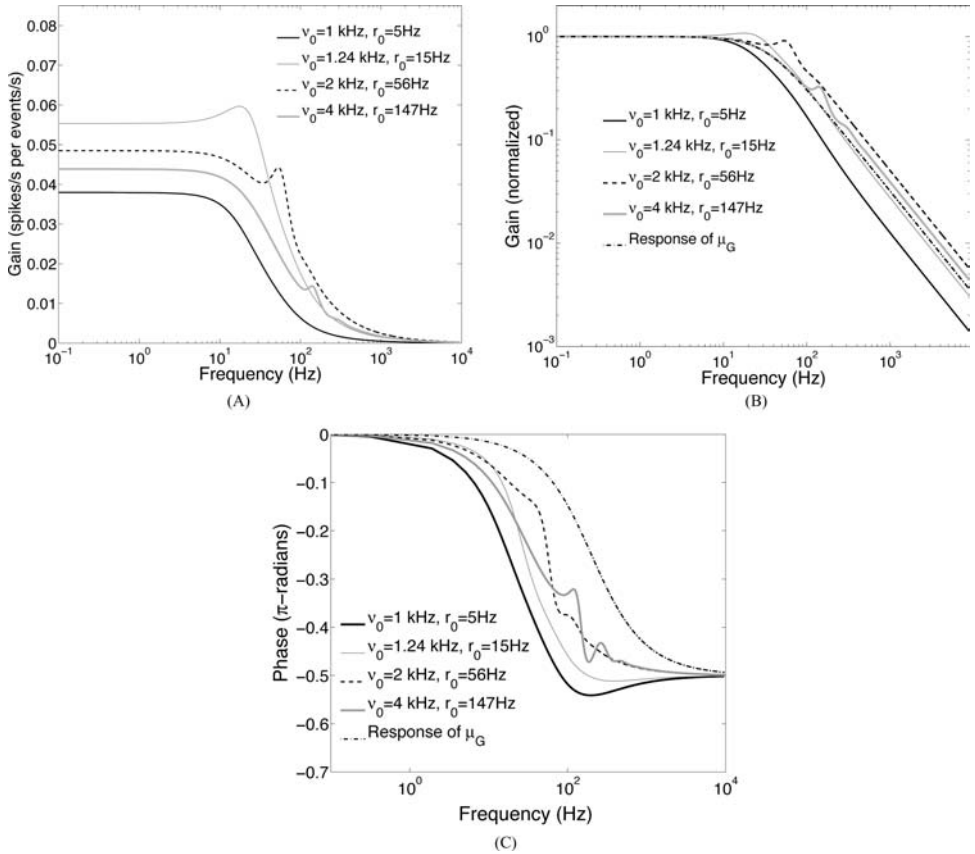


Figure 6. The frequency response of 2-D PDM with excitation only. (A) The gain for various inputs in log-linear coordinates. (B) Gain normalized so  $\mathcal{Z}(0; \nu_0) = 1$  for all curves, in log-log coordinates (Bode-plot format). (C) The phase ( $\pi$ -radians) for various inputs and  $\mu_G$  in log-linear coordinates (Bode-plot). For all plots, the phase asymptotes to  $-0.5 \pi$ -radians ( $-90^\circ$ ). The steady-state output firing rates  $r_0$  for  $\nu_0 = 1$  kHz, 1.24 kHz, 2 kHz, 4 kHz are (respectively): 5 Hz, 15 Hz, 56 Hz, and 147 Hz. Parameters are  $\mathcal{E}_r = -65$  mV,  $v_{th} = -55$  mV,  $\tau_m = 20$  ms,  $\tau_e = 5$  ms,  $\mu_{EPSP} = 0.31$  mV.

when it is superimposed on a particular background synaptic input rate. It is also the case that gain at  $\omega = 0$  is equal to the derivative of the steady firing rate with respect to steady synaptic input rate, i.e.,

$$\mathcal{Z}(0; \nu_0) = \frac{dr_0}{d\nu_0}. \quad (40)$$

Figure 6A shows that absolute gain at  $\omega = 0$ ,  $\mathcal{Z}(0; \nu_0)$ , first increases and then decreases as the background synaptic input rate  $\nu_0$  increases from  $\nu_0 = 10^3$  events/s (giving  $r_0 = 5$  spikes/s) to  $\nu_0 = 4 \times 10^3$  events/s (giving  $r_0 = 147$  spikes/s). According to Equation 40, this is a reflection of the sigmoidal shape of the steady-state input-output curve (not shown) for the 2-D PDF problem. Although there is no refractory period here that would cap the firing rate, the slope of the input-output curve does indeed reach a maximum at an intermediate synaptic input rate, and then decreases a bit thereafter. The difference between the largest and smallest gains at  $\omega = 0$  is roughly 35% of the largest. This behavior also applies to the gains over the range of input modulation frequencies from  $f = 0$  to roughly  $f = 10$  Hz. Figure 6A also shows that the gain for each  $\nu_0$  goes to zero as  $\omega \rightarrow \infty$ . Note that resonant peaks in gain are apparent for the highest 3 background synaptic input rates. For each  $\nu_0$  the peak occurs at a modulation frequency equal to the corresponding background firing rate,  $r_0$  (determined numerically). Knight (2000) and Fourcaud & Brunel (2002) present theoretical discussions of this behavior.

Figure 6B shows in Bode-plot format the corresponding normalized gains, and also shows the normalized gain for the frequency response of the mean synaptic conductance,  $\mathcal{M}_G(\omega)$ . For the population frequency responses, normalized gain for each value of  $\nu_0$  was computed by dividing the absolute gain at each frequency by the gain at  $\omega = 0$ , i.e., normalized gain is given by  $|\mathcal{Z}(\omega; \nu_0)/\mathcal{Z}(0; \nu_0)|$ . Similarly, normalized gain for  $\mu_G$  is given by  $\mathcal{M}_G(\omega)/\mathcal{M}_G(0)$ . Normalized gain at a fixed high frequency provides a rough measure of the “speed” of the transduction, independent of overall gain. Figure 6B show that normalized gain at a fixed high modulation frequency  $f$  first increases, then decreases as the mean synaptic input rate  $\nu_0$  increases from  $\nu_0 = 10^3$  to  $\nu_0 = 4 \times 10^3$  events/s. The difference between largest and smallest gains at a fixed high frequency (e.g.  $f = 1000$  Hz) is roughly 90% of the largest. Normalized gains corresponding to the highest 3 background synaptic input rates differ by roughly a factor of 2 between the largest and smallest among them. It is worth noting that normalized gains for the population firing rates at the highest 2 background synaptic input rates lie above the normalized gain of the mean synaptic conductance. This suggests that the population firing rate can respond “faster” than the mean postsynaptic conductance. This suggestion is supported by inspection of the corresponding impulse responses below.

The asymptotic behavior of the frequency response (Equation 34) as  $\omega \rightarrow \infty$  is determined by the coefficients of  $(\lambda_n + i\omega)^{-1}$  for all  $n \neq 0$ . For this problem, because the coefficients do not sum to zero,  $\mathcal{Z}(\omega; \nu_0)$  decays like  $a(i\omega)^{-1}$  as  $\omega \rightarrow \infty$ , where  $a$  is the sum over all  $n \neq 0$  of the coefficients of  $(\lambda_n + i\omega)^{-1}$  in Equation 33. Thus, the magnitude (gain) decays like  $1/\omega$ , and the phase approaches  $-\pi/2$  (the argument or phase angle of  $a(i\omega)^{-1}$ ). The frequency response of the mean excitatory postsynaptic conductance decays in the same way. Hence, the slopes of the gains on log-log coordinates (Bode-plot format) are all -1 for larger frequencies.

Figure 7A plots the impulse response functions  $z(t; \nu_0)$  corresponding to the frequency responses in Figure 6A. Impulse responses in panel A are on an absolute gain scale. Each impulse response  $z(t; \nu_0)$  can be interpreted as the perturbation in the population firing rate resulting from the arrival of a single additional synaptic event at  $t = 0$ , when it is superimposed on the corresponding mean background synaptic input rate  $\nu_0$ . The impulse responses are

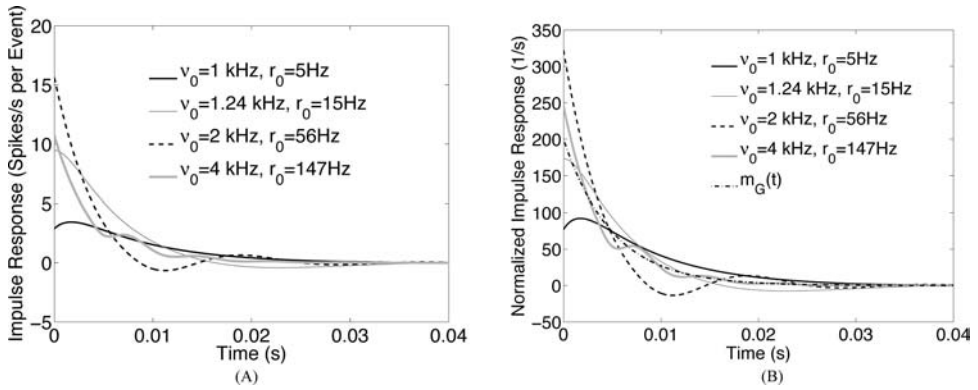


Figure 7. The impulse response of  $r_1$ ; 2-D PDM with excitation only. (A) Impulse response functions for various inputs. (B) Impulse response functions normalized so each curve has unit area. The steady-state output firing rates  $r_0$  for  $v_0 = 1$  kHz, 1.24 kHz, 2 kHz, 4 kHz are (respectively): 5 Hz, 15 Hz, 56 Hz, and 147 Hz. Parameters are the same as in Figure 6.

re-plotted in Figure 7B on a normalized scale; so they correspond to the frequency responses in Figure 6B. This normalization gives a fixed area under the impulse responses across  $v_0$ , so that the change in the total number of spikes elicited by the appropriate number of synaptic events is that same across  $v_0$ . This normalization highlights the differences in population firing rate response kinetics at different background synaptic input rates  $v_0$ .

#### Frequency response and impulse response of 1-D population with excitation only

In the corresponding 1-D PDF problem with excitation only, where the synaptic kinetics are instantaneous (i.e. the limit  $\tau_e \rightarrow 0$ ), the voltage of a neuron jumps instantaneously upon receiving an excitatory synaptic event (Nykamp & Tranchina 2000a). Again, we do not include a refractory period and set  $v_{reset} = \mathcal{E}_r$ . In the 1-D problem, upon the arrival of a unitary postsynaptic conductance event the voltage jumps by an amount  $\Delta v = \Gamma^*(\mathcal{E}_e - v^-)$ , where  $\Gamma^* \equiv 1 - \exp(-A_e/\tau_m)$ ;  $v^-$  is the voltage just before the arrival of the event; and  $A_e$  is the area under the unitary postsynaptic conductance event, as in the 2-D problem. The evolution of the density  $\rho(v, t)$  is governed by (Nykamp & Tranchina 2000a):

$$\frac{\partial \rho}{\partial t} = -\frac{\partial}{\partial v} \left\{ -\frac{1}{\tau_m}(v - \mathcal{E}_r)\rho + v_e(t) \int_{\mathcal{E}_r}^v \tilde{F}_{\Gamma^*} \left( \frac{v - v'}{\mathcal{E}_e - v'} \right) \rho(v', t) dv' \right\},$$

for  $v_{reset} = \mathcal{E}_r \leq v \leq v_{th}$ , (41)

where  $\tilde{F}_{\Gamma^*}$  is the complementary cumulative distribution function of the random variable  $\Gamma^*$ . The boundary conditions are  $\mathcal{F}_V(v_{th}, t) = \mathcal{F}_V(\mathcal{E}_r, t)$ , and  $\rho(v_{th}, t) = 0$ , where

$$\mathcal{F}_V(v, t) = -\frac{1}{\tau_m}(v - \mathcal{E}_r)\rho + v_e(t) \int_{\mathcal{E}_r}^v \tilde{F}_{\Gamma^*} \left( \frac{v - v'}{\mathcal{E}_e - v'} \right) \rho(v', t) dv'$$

is the probability flux. The population firing rate  $r(t)$  is given by the probability flux evaluated at threshold voltage,  $\mathcal{F}_V(v_{th}, t)$ . Because of the zero density boundary condition at  $v_{th}$  the advective component of the probability flux does not contribute to the firing rate. Therefore, the firing rate is given by

$$r(t) = v_e(t) \int_{\mathcal{E}_r}^{v_{th}} \tilde{F}_{\Gamma^*} \left( \frac{v_{th} - v'}{\mathcal{E}_e - v'} \right) \rho(v', t) dv' \quad (42)$$

For the corresponding discretization of this problem, the firing rate is given by

$$r(t) = v_e(t) \vec{b}^1 \cdot \vec{\rho}(t), \quad (43)$$

where  $\vec{b}^1 \cdot \vec{\rho}(v, t)$  is a discretization of

$$\int_{\mathcal{E}_r}^v \tilde{F}_{\Gamma^*} \left( \frac{v - v'}{\mathcal{E}_e - v'} \right) \rho(v', t) dv'.$$

The expression for the first order density term ( $\vec{\rho}_1$ ) is exactly of the same form for the 1-D and 2-D problems, but the expression for the firing rates differ. For sake of easily distinguishing between the 1-D and 2-D problems below, we will use the superscript 1 to denote 1-D for emphasis in some places. For the 1-D problem,

$$r_0 = v_0 \vec{b}^1 \cdot \vec{\rho}_0, \quad (44)$$

and

$$r_1(t) = v_1(t) \vec{b}^1 \cdot \vec{\rho}_0 + v_0 \vec{b}^1 \cdot \vec{\rho}_1(t). \quad (45)$$

Consequently, the frequency response (computed by following the same strategy used for the 2-D problem) is given by

$$\mathcal{Z}^1(\omega; v_0) = \vec{b}^1 \cdot \vec{\rho}_0 + v_0 \vec{b}^1 \cdot \left( (i\omega I - \mathcal{Q}^1(v_0))^{-1} \frac{d\mathcal{Q}^1}{dv} \vec{\rho}_0 \right) \quad \text{for } \omega \neq 0, \quad (46)$$

$$= \vec{b}^1 \cdot \vec{\rho}_0 + v_0 \sum_{n \neq 0} \frac{\left( \vec{\phi}_n^*, \frac{d\mathcal{Q}^1}{dv} \vec{\rho}_0 \right) (\vec{b}^1, \vec{\phi}_n)}{i\omega - \lambda_n} \quad (47)$$

where,  $\mathcal{Q}^1(v) \cdot \rho$  is the discretization of the right-hand-side of 41, and  $\frac{d\mathcal{Q}^1}{dv} \cdot \rho$  is the discretization of

$$-\frac{\partial}{\partial v} \left\{ \int_{\mathcal{E}_r}^v \tilde{F}_{\Gamma^*} \left( \frac{v - v'}{\mathcal{E}_e - v'} \right) \rho(v', t) dv' \right\}.$$

An important observation in Equation 47 is that the first term  $\vec{b}^1 \cdot \vec{\rho}_0$  is a real, positive number, and independent of the frequency,  $\omega$ , while the second term approaches 0 as  $\omega \rightarrow \infty$ . Consequently, the gain does not approach 0 as  $\omega \rightarrow \infty$ ; instead it approaches  $\vec{b}^1 \cdot \vec{\rho}_0$ , which is in contrast to the 2-D case (see Figure 6). This result for conductance-driven synapses in the 1-D problem is similar to that reported by (Knight 2000) for current-driven synapses in the corresponding 1-D problem.

As in the 2-D case, we calculate the impulse response function  $z(t; v_0)$  by taking the inverse Fourier transform of  $\mathcal{Z}^1(\omega; v_0)$  in Equation 47 to obtain (see Figure 9):

$$z^1(t; v_0) = (\vec{b}^1, \vec{\rho}_0) \delta(t) + \left[ v_0 \sum_{n \neq 0} \left( \vec{\phi}_n^*, \frac{d\mathcal{Q}^1}{dv} \vec{\rho}_0 \right) (\vec{b}^1, \vec{\phi}_n) e^{\lambda_n t} \right] H(t). \quad (48)$$

Equation 48 implies that a delta function (impulse) input in synaptic input rate will generate a population firing rate response that has a delta function component. Figure 8 plots the 1-D frequency response. Notice Figures 6A and 8A, as well as Figures 6B and 8B, have the same scale for the vertical (gain) axis.

The format of the frequency responses for the 1-D problem (instantaneous synaptic kinetics) in Figures 8A, B and C are the same as those for the 2-D problem above (Figure 6).



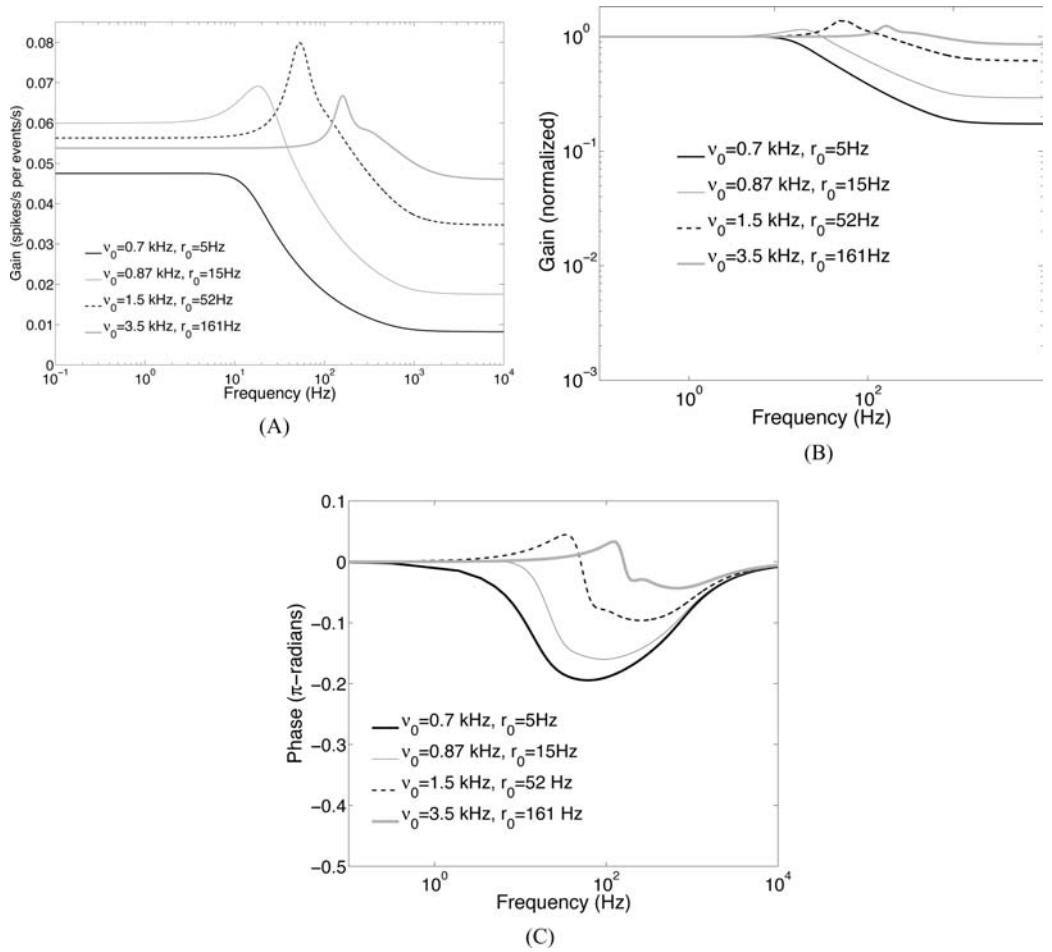


Figure 8. The frequency response of 1-D PDM with excitation only. (A) The gain for various inputs in log-linear coordinates. (B) Gain normalized so  $\mathcal{Z}(0; v_0) = 1$  for all curves, in log-log coordinates (Bode-plot format). (C) The phase ( $\pi$ -radians) for various inputs in log-linear coordinates (Bode-plot). For all inputs  $v_0$ , the phase asymptotes to 0. The steady-state output firing rates  $r_0$  for  $v_0 = 0.7$  kHz, 0.87 kHz, 1.5 kHz, 3.5 kHz are (respectively): 5 Hz, 15 Hz, 52 Hz, and 161 Hz. Parameters are  $\mathcal{E}_r = -65$  mV,  $v_{th} = -55$  mV,  $\tau_m = 20$  ms,  $\mu_{EPSP} = 0.5$  mV for  $v^- = \mathcal{E}_r$ .

The behavior of the frequency responses at low frequencies is similar for the 1-D and 2-D problems. The behavior at high frequencies is dramatically different because of the the high-frequency horizontal asymptote for the gain in the 1-D problem. The corresponding phase lags in Figure 8C all have a horizontal asymptote of 0 rad. Furthermore, in the 1-D problem, absolute and normalized gain at a fixed high temporal frequency (e.g.  $f = 200$  Hz) both increase monotonically as the background synaptic input rate  $v_0$  is increased from  $0.7 \times 10^3$  to  $3.5 \times 10^3$  events/s.

The impulse responses in Figures 9A and B correspond to the frequency responses in Figures 8A, B and C. The Dirac  $\delta$ -function components can not be plotted explicitly, but they are represented symbolically in the figures. As in the 2-D problem above, response kinetics speed up with increasing background synaptic input rate  $v_0$ .

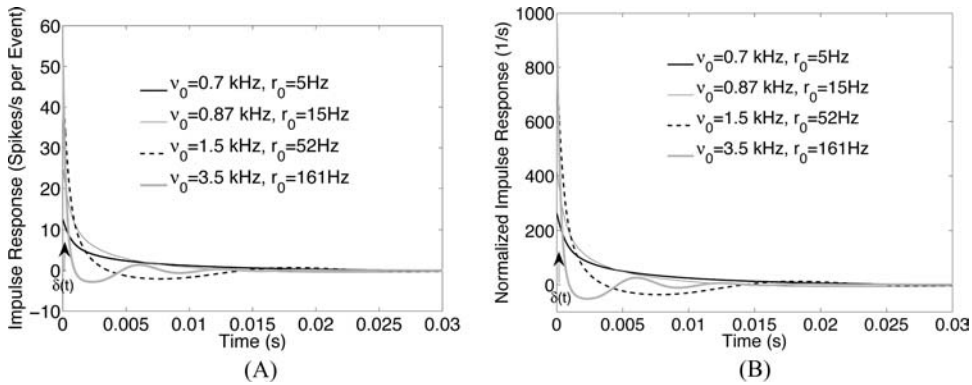


Figure 9. The impulse response of  $r_1$ ; 1-D PDM with excitation only. (A) Impulse response functions for various inputs. (B) Impulse response functions normalized so each curve has unit area. The steady-state output firing rates  $r_0$  for  $v_0 = 0.7$  kHz, 0.87 kHz, 1.5 kHz, 3.5 kHz are (respectively): 5 Hz, 15 Hz, 52 Hz, and 161 Hz. Parameters are the same as in Figure 8.

## Inhibitory synaptic conductance

In this section, we show results with the addition of the inhibitory synaptic conductance using mean-field approximation for the inhibitory postsynaptic conductance random variable, as in Nykamp & Tranchina (2000b). They showed that using the mean-field value of the inhibitory conductance random variable in the population evolution equation requires only the assumption that the mean of the inhibitory conductance is independent of voltage. It does not require the more restrictive assumption (approximation) that all neurons in the postsynaptic population have the same deterministic inhibitory conductance. This is the most elementary method to reduce the dimension of the population density function state space, with the addition of inhibition, from 3 to 2.

### Mean-field inhibition

With the mean-field inhibition approximation Equation 2 is modified to become

$$\tau_m \frac{dV}{dt} + (V - \mathcal{E}_r) + G_e(t)(V - \mathcal{E}_e) + \mu_{G_i}(t)(V - \mathcal{E}_i) = 0, \quad (49)$$

keeping the state-variables down to two, namely  $V$  and  $G_e$ .

The mean-field inhibitory conductance  $\mu_{G_i}$  is obtained by solving the following differential equation at every time-step, as is explained in Appendix A of Nykamp & Tranchina (2000b).

$$\frac{d\mu_{G_i}}{dt} = \frac{v_i(t)\mu_{A_i} - \mu_{G_i}(t)}{\tau_i}, \quad (50)$$

where  $\mu_{A_i}$  is the mean of the area under the unitary inhibitory postsynaptic conductance waveform.

When mean-field inhibition is added in the population density method, the voltage operator becomes time dependent (Equations 49 and 50) (and remains excitatory-conductance dependent). Recomputing this time dependent operator at every time step does not slow the numerical simulations considerably. Furthermore, the strength of the inhibition and excitation does not play a role in the computational time of the population density simulations.

On the contrary, the Monte–Carlo simulations take longer with stronger excitation and/or inhibition, because the number of synaptic events increases.

In this section, we show some results using mean-field inhibition for different values for  $\mu_{A_i}$  and  $\tau_i$ . Each choice corresponds to a different mean IPSP size at peak time ( $\mu_{IPSP}$ ), which we computed for two different voltage initial conditions:  $v(0) = \mathcal{E}_r$ , and  $v(0) = v_{th}^-$  (see Appendix D). We also show how deficiencies of the mean-field approximation for inhibition can be more dramatic in a network setting in which there are feedback loops.

### Single population with mean-field inhibition

For a single population we ran a barrage of simulations for different external inhibitory synaptic input and we observed that the PDM with mean-field inhibition was a good approximation for most inputs and for the  $\mu_{A_i}$  and  $\tau_i$  used in these simulations (one shown on left column of Figure 10). We then tested the role of the mean unitary inhibitory postsynaptic potential  $\mu_{IPSP}$  and decay time constant  $\tau_i$  in the accuracy of our PDM with the mean-field inhibition approximation, while the excitatory time constant  $\tau_e = 5$  ms and mean unitary

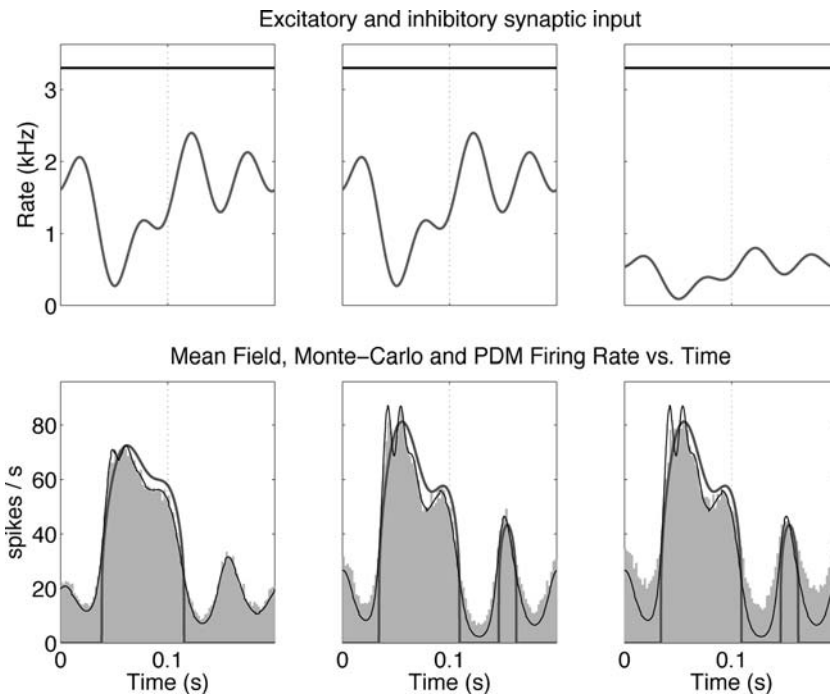


Figure 10. Single uncoupled population dynamics with excitatory and inhibitory synaptic input for 3 different sets of inhibition parameters. The excitatory and inhibitory synaptic input rates are shown for the 3 experiments in the upper panels. The excitatory synaptic input was the same in all 3 cases. The inhibitory synaptic input rates are scaled versions of a common waveform. The scaling depends on the unitary inhibitory conductance parameters and keeps the average inhibitory conductance (averaged over population and time) constant across experiments. For the left column the parameters were ( $\tau_i = 15$  ms,  $\mu_{A_i} = 7.7 \times 10^{-4}$  s,  $\mu_{IPSP}$  equal to 0.08 and 0.19 mV for  $v(0)$  equal to  $\mathcal{E}_r$  and  $v_{th}^-$ , respectively). For the middle column, only  $\tau_i$  was changed by decreasing it from 15 ms to 5 ms (same as  $\tau_e$ ), giving  $\mu_{IPSP}$  equal to 0.12 and 0.32 mV for  $v(0)$  equal to  $\mathcal{E}_r$  and  $v_{th}^-$ , respectively. In the right column,  $\tau_i$  was kept at 5 ms while  $\mu_{A_i}$  was increased by a factor of 3 from  $7.7 \times 10^{-4}$  s to  $2.3 \times 10^{-3}$  s, while the rate of inhibitory synaptic input was decreased by a factor of 3, giving  $\mu_{IPSP}$  equal to 0.35 and 0.93 mV for  $v(0)$  equal to  $\mathcal{E}_r$  and  $v_{th}^-$ , respectively. The PDM with mean-field inhibition is a better approximation for the smaller and slower IPSPs.

excitatory conductance were held fixed. One can increase the mean IPSP by either using a faster inhibitory synaptic time constant  $\tau_i$  and/or by increasing the mean area under the unitary event conductance waveform  $\mu_{A_i}$ .

Figure 10 compares performance of the PDM with the mean-field inhibition approximation for 3 sets of parameters all giving the same mean inhibitory conductance when the averaging is done over population and time. For the left column the parameters were ( $\tau_i = 15$  ms,  $\mu_{A_i} = 7.7 \times 10^{-4}$  s,  $\mu_{IPSP}$  equal to 0.08 and 0.19 mV for  $v(0)$  equal to  $\mathcal{E}_r$  and  $v_{th}^-$ , respectively). For the middle column, only  $\tau_i$  was changed by decreasing it from 15 ms to 5 ms (same as  $\tau_e$ ), giving  $\mu_{IPSP}$  equal to 0.12 and 0.32 mV for  $v(0)$  equal to  $\mathcal{E}_r$  and  $v_{th}^-$ , respectively. In the right column,  $\tau_i$  was kept at 5 ms while  $\mu_{A_i}$  was increased by a factor of 3 from  $7.7 \times 10^{-4}$  s to  $2.3 \times 10^{-3}$  s, while the rate of inhibitory synaptic input was decreased by a factor of 3, giving  $\mu_{IPSP}$  equal to 0.35 and 0.93 mV for  $v(0)$  equal to  $\mathcal{E}_r$  and  $v_{th}^-$ , respectively.

Figure 10 shows that in the case of external inhibitory and excitatory input to a single uncoupled population the PDM with mean-field inhibition approximation for the inhibitory conductance random variable does work well when the IPSP is 3 times smaller than the EPSP (or more) and the inhibitory time constant is 3 times larger than the excitatory time constant. However, the method is not accurate at low firing rates (below 25 Hz or so) when the EPSP and the IPSP have similar size and kinetics.

#### Mean-field inhibition in neural networks

We tested our mean-field inhibition methods in two simple networks, each containing two populations. In both cases, inhibitory synaptic input is generated within the network.

*Feed-forward connectivity.* To test the performance of our PDM in a network with feed-forward inhibition, we set up simple two-population networks. Figure 11 shows results from an

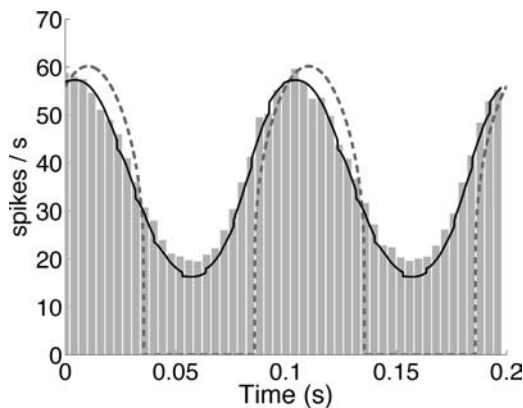


Figure 11. Firing rate of excitatory population in inhibitory-excitatory feed-forward network. Comparison between Monte-Carlo simulations (grey histogram), full mean-field approach (dashed line) and probability density with mean-field inhibition approximation. The inhibitory population receives synaptic input modulated with a sine wave with mean 2000 Hz and 20% contrast. The excitatory population receives constant external synaptic input at 4000 Hz. Excitatory neurons receive an average of 40 inhibitory synaptic inputs per neuron. The Monte-Carlo simulations (shaded light grey bars) were run with 100 neurons per population averaged over 100 realizations. Parameters:  $dt = \tau_e/20$ ;  $\mu_{A_e} = 1.538 \times 10^{-4}$  s;  $\mu_{A_i} = 7.692 \times 10^{-4}$  s;  $\mu_{EPSP} = 0.31$  mV and  $\mu_{IPSP} = 0.08$  mV with initial condition  $v(0) = \mathcal{E}_r$ ;  $\mu_{IPSP} = 0.19$  mV with initial condition  $v(0) = v_{th}^-$ .

example in which the inhibitory population A receives temporally modulated external excitatory synaptic input, and it inhibits population B which receives constant external excitatory synaptic input. The firing rate of population B (the inhibited population) is shown in Figure 11 for a simulation in which each neuron is receiving an average of 40 inhibitory synapses from population A. In these simulations the parameters for the unitary postsynaptic conductance event were the same as those used in Figure 10, left column. Figure 11 shows good agreement between the Monte–Carlo and PDM results. In simulation such as these, we found no evidence for any difference in performance between externally and internally generated inhibition for feed-forward connectivity.

*Feedback connectivity.* We set up a network with inhibitory feedback connectivity to test the performance of the mean-field inhibition in this situation. The motivation came from the work of Haskell et al. (2001), who showed that their dimension reduction method gave particularly poor results in some feedback networks. It appears that errors stemming from dimension reduction approximations can be grossly magnified by feedback (Haskell et al. 2001).

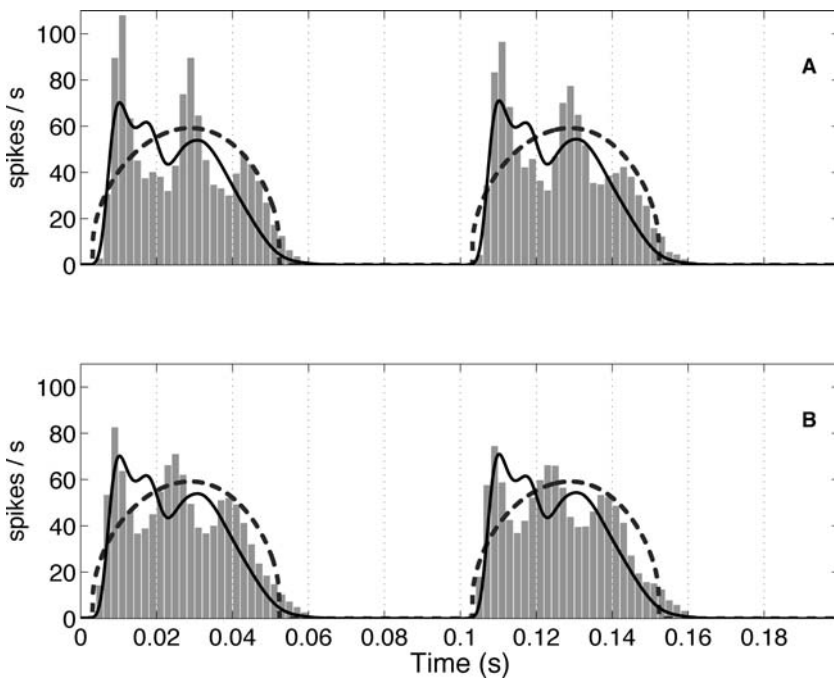


Figure 12. Two population excitatory-inhibitory network with feedback connectivity. Comparison between Monte–Carlo simulations (grey histogram), full mean-field approach (dotted grey line) and probability density with mean-field inhibition (black line). The excitatory population firing rate is shown for simulations with 50 neurons in each population (panel A) and 1000 neurons in each population (panel B). In panel A, the Monte–Carlo simulations with 50 neurons per population were averaged over 100 realizations; in panel B, simulations with 1000 neurons were averaged over 20 realizations. The connectivity is fairly dense in panel A but sparse in panel B. The excitatory population receives external synaptic input with mean 2000 Hz and modulated with a sinusoidal time course with 10 Hz frequency and contrast of 0.5. Inhibitory neurons receives an average of 35 excitatory synapses per neuron; excitatory neurons receive an average of 25 inhibitory synapses per neuron. Parameters:  $dt = \tau_e/40$ ,  $\mu_{A_e} = 1.538 \times 10^{-4}$  s,  $\mu_{A_i} = 7.692 \times 10^{-4}$  s,  $\mu_{EPSP} = 0.31$  mV,  $\mu_{IPSP} = 0.08$  mV with initial condition  $v(0) = \mathcal{E}_r$  and  $\mu_{IPSP} = 0.19$  mV with initial condition  $v(0) = v_{th}^-$  (see Appendix D).

Figure 12 shows the firing rate of the inhibitory population in a 2-population network with one excitatory and one inhibitory population. The parameters for the inhibitory synaptic events are those that gave excellent results in the cases of external inhibitory synaptic input (Figure 10, left panel) and in the case of feed-forward inhibitory synaptic input above. Panels A and B correspond to dense and sparse connectivity, respectively. In both cases deficiencies of the mean-field inhibition approach are evident in the context of feedback connectivity.

In this example, only the excitatory population receives external synaptic input with a mean rate of 2000 Hz and a sinusoidal modulation around the mean with contrast of 0.5. Every neuron in the inhibitory population receives input from 35 excitatory neurons on average. Neurons in the excitatory population receive input from 25 inhibitory neurons on average. The top and bottom panels show results with 50 and 1000 neurons per population, respectively. The population density method captures some features of the population response dynamics of the direct MC simulations even at the high connectivity (panel A), but there are substantial discrepancies both for the dense and sparse connectivity cases. In panel A, both high connectivity and the mean-field inhibition approximation contribute to the error, but in panel B the only significant source of the substantial error is the mean-field approximation for inhibition.

## Summary and discussion

We have developed and explored a 2 dimensional state-space population density method for modeling large groups of interacting neurons with realistic synaptic kinetics. Our work extends computational methods developed previously (Knight 1972a, 1972b; Knight et al. 1996, 2000; Omurtag et al. 2000; Nykamp & Tranchina 2000a, 2000b; Nykamp 2000, Haskell 2000). Population density methods have been used previously as a time saving computational tool in a 2-D state space for an integrate-and-fire-or-burst model neuron (Casti et al. 2002; Huertas & Smith 2006); in that case, the slow dynamic variable is a calcium conductance variable. Others (Fourcaud & Brunel 2002; Moreno-Bote & Parga 2004; 2005) have studied 2-D population density problems similar to ours, where the density evolves via a Fokker-Planck equation. Assuming the synaptic and membrane time constants are on disparate scales, they derive asymptotic expansions for the steady-state 2-D density and the output firing rate that give good results even when the time-scales are not disparate.

We devised a second-order accurate numerical methods using operator splitting for solving the partial differential-integral equations that describe the evolution of two coupled 2-D probability density functions. We found the operator splitting method to be 6 times faster than a single operator method (Appendix A). There is a difference between the phase space of our problem and that of Casti et al. (2002) that required them to use a total-variation-diminishing numerical scheme, rather than a scheme like ours. That is the purely advective nature of the slow calcium conductance component of the probability flux, which can cause a build-up of probability at either extreme values (0 or 1) of that variable (Casti et al. 2002).

We tested our population density method against a mean-field method and against direct Monte-Carlo simulations with individual neurons for various networks. We have shown that the population density approach in a 2-D state space is an efficient and accurate method to describe the dynamics of networks of excitatory neurons with realistic synaptic kinetics.

We found that using 28 voltage and conductance bins gave good results (rms error of 2%) when using a mean EPSP of 0.31 mV and a distance of 10 mV from rest to threshold voltage. Increasing the number of voltage and conductance bins gave essentially no improvement in the agreement between population density results and Monte-Carlo results for a single uncoupled population with 100,000 neurons.



The population density method was used to analyze population firing rate kinetics (frequency response and impulse response functions) in two I&F neuron models with conductance-driven synapses, one with realistic synaptic kinetics (2-D), and one with instantaneous synaptic kinetics (1-D).

The addition of inhibition in the form of a mean-field approximation for the inhibitory conductance random variable allowed us to retain a 2-dimensional state-space. The only change in the PDM when adding inhibition is that the voltage operator becomes time dependent. The addition of time dependence in the voltage operator does not slow the numerical simulations much for the population density runs. We found that the mean-field inhibition method works especially well in networks with feedforward connectivity, and with parameters that give small and slow unitary postsynaptic conductance events. However, the method can break down in feedback networks, even with sparse connectivity and parameters that give good results with feed-forward connectivity (Figure 12).

#### *Frequency response comparison with Fourcaud & Brunel (2002), Brunel et al. (2001)*

We considered the dynamics of the transduction in which rate of postsynaptic conductance events is the input, and population firing rate is the output, as in Knight (2000). We have shown that when realistic synaptic conductances are modeled (2-D PDM with excitation only), the frequency response of an uncoupled population of identical neurons is dramatically different from that in the instantaneous synaptic kinetics case (1-D PDM with excitation only). With realistic synaptic kinetics, the frequency-response gain goes to 0 as the frequency goes to  $\infty$ , and the phase asymptotes to  $-\pi/2$  radians. The corresponding impulse response function does not have an instantaneous (delta function) component. In the case of instantaneous synaptic kinetics, the gain asymptotes to a positive value as the frequency goes to  $\infty$ , and the phase asymptotes to 0 radians. The corresponding impulse response function has an instantaneous (delta function) component. Knight (2000) obtained this result previously for I&F neurons with current-driven synapses in the case of instantaneous synaptic kinetics.

The contrasting behavior of the two impulse response functions can be easily understood by physical reasoning. The impulse response function in our problem gives the change in population firing rate per unitary postsynaptic conductance event superimposed on top of a background rate of events. In the 2-D (non-instantaneous synaptic kinetics) case, a single unitary event causes an instantaneous jump in the synaptic conductance of a neuron, but not in the membrane voltage. The probability flux across threshold voltage is advective in the 2-D case. Consequently, if neurons in the population receive an excess synaptic event at  $t = 0$ , the population firing rate jumps instantaneously by a finite amount between  $t = 0^-$  and  $t = 0^+$ , but no probability crosses threshold in this time interval. The total probability crossing threshold over any time interval is given by the integral of the probability flux, and the integral over an interval of zero width is always zero in this case. In the 1-D (instantaneous synaptic kinetics) case, in contrast, a single unitary event causes an instantaneous jump in membrane voltage. The size of the jump is determined by the area under the unitary postsynaptic conductance event (coefficient of the delta function synaptic conductance time course). Any neuron close enough to threshold when the excess postsynaptic event arrives will jump across threshold. Therefore, a non-zero fraction of the population will fire instantaneously. This accounts for the delta function component of the impulse response function; the continuous component is determined by the evolution of the probability density function thereafter as the population relaxes to its steady state.

Fourcaud & Brunel (2002), Brunel et al. (2001) analyzed the frequency response of neurons with current injection input. The current injection they considered has a background

component  $I_{in}(t) = I_0 + I_1 \cos(\omega t)$  with superimposed noise.

$$I(t) = I_{in}(t) + I_{noise}(t), \quad (51)$$

where

$$\tau_s \frac{dI_{noise}(t)}{dt} = \eta(t) - I_{noise}(t). \quad (52)$$

They considered two types of  $I_{noise}(t)$ : colored noise where  $\tau_s > 0$  in Equation 52 (analogous to our 2-D PDM) and white noise where  $\tau_s = 0$  in Equation 52 (analogous to our 1-D PDM).

The asymptotic behaviors (as  $\omega \rightarrow \infty$ ) they obtained for instantaneous versus non-instantaneous synaptic kinetics are the reverse of ours because the two problems are physically different. For colored noise, that mimics background synaptic input with non-instantaneous synaptic kinetics, their gain asymptotes to a positive value with a phase that approaches 0 radians. For white noise, that mimics background synaptic input with instantaneous synaptic kinetics, their gain decreases like  $1/\sqrt{\omega}$ , as the frequency,  $\omega$ , goes to  $\infty$ ; the phase approaches  $-\pi/4$  radians as  $\omega \rightarrow \infty$ . Fourcaud & Brunel (2002) have already pointed out that in real neurons receiving input through synapses, there is additional temporal filtering by the kinetics of synaptic conductance. These authors (Fourcaud & Brunel 2002; Brunel et al. 2001) have explained very well why their results make sense physically, but for sake of completeness we make a few explanatory comments along the lines above for our different problem. When injected current is the input, a delta function of current that delivers a total charge  $Q$  will cause an instantaneous jump in the voltage  $Q/c$ , where  $c$  is the membrane capacitance, both in the 1-D (white background current noise) and 2-D (colored background current noise). The different behavior between 1-D and 2-D (white versus colored noise) can be explained as follows. If the charge is order  $\epsilon$  in the colored noise case, both the jump in membrane voltage and the total probability jumping across threshold instantaneously will also be of order  $\epsilon$ , because the probability density function at threshold and in its vicinity is non-zero. In the white noise case, although the jump in voltage is still of order  $\epsilon$ , the total probability jumping across threshold instantaneously will be of order  $\epsilon^2$  as a consequence of the zero boundary condition on the probability density function at threshold. The impulse response function, by its definition, gives the order  $\epsilon$  component of the response for an order  $\epsilon$  input superimposed on a background. In the white noise case, the order  $\epsilon$  component is zero. In a practical MC simulations, with delta function current injection, one would measure an instantaneous component of the population firing rate in both the white noise and colored noise cases. However, for small total charge  $Q$  injected, the fraction of neurons firing instantaneously would scale as  $Q$  in the colored noise case, but as  $Q^2$  in the white noise case.

In Figures 8B and 8C, there is a range of intermediate frequencies (roughly 20 Hz–200 Hz) where the curve corresponding to  $r_0 = 5$  Hz looks like those in the white noise problem of Fourcaud & Brunel (2002), Brunel et al. (2001): gain with slope of  $-1/2$  in Bode-plot, phase approaching  $-0.25 \pi$ -rad. When  $\mu_A \ll 1$ , the Taylor series approximation  $\rho(v', t) \approx \rho(v, t) + \partial \rho(v, t) / \partial v (v' - v)$  in Equation 41 is quite good (Nykamp & Tranchina 2000a). This leads to a drift-diffusion equation that has a similar form as the white noise problem. As  $\mu_A$  gets smaller and  $v_0$  larger, one might expect the range of frequencies with the white noise behavior to increase. We verified this numerically (not shown), but the gain still asymptotes to a nonzero value for large frequencies as long as  $\mu_A > 0$ . This phenomena can be understood as follows: for the sake of simplicity, we ignore the voltage dependent correction terms that play a role only near  $\mathcal{E}_r$  in the advection-diffusion approximation of (Nykamp & Tranchina

2000a):

$$\frac{\partial \rho}{\partial t} = -\frac{\partial}{\partial v} \left\{ -\frac{1}{\tau_m} [(v - \mathcal{E}_r) + v_e(t) \mu_A (v - \mathcal{E}_e)] \rho - \frac{v_e(t) \mu_A (\mathcal{E}_e - v)^2}{2\tau_m} \frac{\partial \rho}{\partial v} \right\}.$$

Linearizing  $v_e(t)$ , and  $\rho(t)$  as before, the equation for the first order component of density is:

$$\begin{aligned} \frac{\partial \rho_1}{\partial t} = & -\frac{\partial}{\partial v} \left\{ -\frac{1}{\tau_m} [(v - \mathcal{E}_r) + v_0 \mu_A (v - \mathcal{E}_e)] \rho_1 \right\} - \frac{\partial}{\partial v} \left\{ -\frac{1}{\tau_m} v_1(t) \mu_A (v - \mathcal{E}_e) \rho_0 \right\} \\ & + \frac{\partial}{\partial v} \left\{ \frac{v_0 \mu_A (\mathcal{E}_e - v)^2}{2\tau_m} \frac{\partial \rho_1}{\partial v} \right\} + \frac{\partial}{\partial v} \left\{ \frac{v_1(t) \mu_A (\mathcal{E}_e - v)^2}{2\tau_m} \frac{\partial \rho_0}{\partial v} \right\}, \end{aligned} \quad (53)$$

The frequency response has the same form as Equation 47:

$$\mathcal{Z}^1(\omega; v_0) = \vec{b}^{\dagger} \cdot \vec{\rho}_0 + v_0 \sum_{n \neq 0} \frac{(\vec{\phi}_n^*, \frac{dQ^1}{dv} \vec{\rho}_0) (\vec{b}^{\dagger}, \vec{\phi}_n)}{i\omega - \lambda_n}.$$

The horizontal asymptote in the frequency response and the delta function component of the corresponding impulse response are due to the frequency-independent last term in Equation 53. As  $\mu_A$  decreases (consequently  $\mu_A$  decreases) the diffusion approximation gets better. If we increase  $v_0$  so that  $r_0$  is fixed, the delta function component  $(\vec{b}^{\dagger} \cdot \vec{\rho}_0)$  gets smaller because  $\vec{b}^{\dagger} \cdot \vec{\rho}_0 = r_0/v_0$ . Ignoring the last term in Equation 53 results in an equation like that in Fourcaud & Brunel (2002), Brunel et al. (2001), corresponding to the white noise background and deterministic current injection input problem. However, it is important to note that in our problem, in the small  $\mu_A$  regime, the power of equivalent white noise and the magnitude of the deterministic conductance drive are linked and cannot be tuned independently. The noise power necessarily decreases as  $\mu_A$  is made smaller.

#### *Other possible applications of 2-D population density methods*

The 2-D population density methods could be applied to a model neuron with fast excitation and slow inhibition. If we assume that the excitatory time constant is much shorter than the membrane time constant (Nykamp & Tranchina 2000b), we can replace the unitary excitatory conductance waveform with a delta function of magnitude equal to the integral of the original conductance change. If we then add full slow inhibition, voltage and inhibitory conductance would be the two state variables. This application would involve similar methodologies to those we have been using for a model with realistic synaptic kinetics. The voltage component of the probability flux vector would have an advection part from leakage and an integral part from jumps in voltage upon arrival of the excitatory synaptic events. The inhibitory conductance operator would, on the other hand, take the shape that our excitatory conductance operator has in our present model.

Another possible application is to neurons with instantaneous synaptic kinetics and synaptic depression. The synaptic depression state variable for a neuron's synaptic terminal would jump downward every time a spike arrives at the terminal and successful synaptic transmission occurs, and would evolve towards 1 with an exponential time course in between synaptic transmission events. The synaptic depression variable of a synaptic terminal would determine the probability of synaptic release from that terminal.

*Practicality of the PDM and need for dimension reduction methods*

Because synaptic kinetics play such an important role in network dynamics (see Introduction for references), population density methods will not be widely applicable until synaptic kinetics can be modeled accurately in this method. Inhibition, in addition to excitation, could be treated properly by adding a third state variable for the random inhibitory conductance in the population density function. Exact numerical solution of the resulting evolution equation would certainly be slower than the corresponding direct Monte–Carlo method. Therefore, reliable and accurate dimension reduction methods need to be developed.

The fact that inhibitory synaptic kinetics are often slower than excitatory synaptic kinetics motivated Nykamp and Tranchina (Nykamp & Tranchina 2000b) to extend their integrate-and-fire population density method for the case of instantaneous synaptic kinetics to account for slower inhibition. They used a moment closure technique (closing at the first moment), like the one we used here, to reduce the dimension of state-space back to one. The method assumes that the mean of the inhibitory conductance is independent of the membrane voltage. In this way, the computational efficiency was conserved and little accuracy was lost by that assumption. However, we found that this method does not work nearly as well, particularly in the context of feedback connectivity, when excitation and inhibition are not on disparate time scales.

Haskell et al. (2001) used a different dimension reduction method to obtain an approximation of the dynamics of the probability density when both the excitation and inhibition are provided by current injection rather than conductance modulation. The method applies to all cases in which the unitary postsynaptic current events can be expressed by a sum of exponentials. This was an ad-hoc method that was shown to give poor results in some situations.

Haskell et al. (2001) suggested a dimension reduction method based on a moment closure technique that is a generalization of that used in (Nykamp & Tranchina 2000b). The key idea in the case of excitatory input only, for example, is the assumption that the  $k^{th}$  centered moment of the synaptic conductance is independent of membrane potential. Cai et al. (2004, 2006) used such a moment closure technique to obtain a one dimensional kinetic theory that they compared to direct simulations in a model for primary visual cortex. Ly & Tranchina (2006) have found that this method, with physiological parameters, when properly implemented numerically, breaks down at synaptic input rates that are even higher than the threshold rate for the full mean-field method. The synaptic input rate where this dimension reduction method fails can correspond to correct output firing rates higher than 59 Hz. The failure stems from the fact that the moment closure equations give an ill-posed problem, in the sense that no solution of any kind exist, for a wide range of physiological parameters (Ly & Tranchina 2006). It is also possible that other moment closures could be derived—along the lines of Chapman–Enskog methods (Chapman & Cowling 1970)—that would work well for 2-D and higher dimensional population density methods.

A dimension reduction method based on principal components analysis has been shown to work well in the one dimensional population density problem for neurons with instantaneous synaptic kinetics (Knight 2000). It is possible that this method could be extended to higher dimensions.

Knight et al. (2000) derived an exact theoretical expressions for the density and firing rate response of a population of neurons that receive a step change in the rate of postsynaptic current input events. We have implemented this method for our formulation of the 1-D PDM, and successfully generalized this method by including a refractory period and allowing dynamic input (see Appendix A). We have also successfully extended this computationally

efficient method to our 2-D PDM (Appendix A), again with a refractory period and dynamic input. However, we found this method to be only three times faster than the operator splitting method (Appendix A). Operator splitting may be extended to higher dimensions, but not without modifications and higher order fractional time steps (Khan & Liu 1998). The eigenvector expansion method might hold more promise because in principle, it can be easily extended to higher dimensions. However, computing eigenvectors of operators for 3 or higher dimensions might not be practical.

### *Concluding remarks*

The fact that our 2-D population density method (operator splitting) is roughly 30 times faster than direct Monte–Carlo simulations in single uncoupled population simulations (with rms error of 2%) might make it a useful and practical tool for simulating activity in networks of excitatory neurons. The computational advantage of the PDM grows with the number of populations in neural network simulations. It is likely that even faster numerical methods could be developed.

The problem with the probability density method as a time-saving computational tool lies in the introduction of other state variables—such as inhibitory postsynaptic conductance and a synaptic depression state variable—that are necessary to make a realistic underlying single neuron.

We can make a rough estimate of how the computation time would increase with the introduction of a third state variable. We found that in going from a 1-D problem to a 2-D problem the computation time required for a fixed number of time steps increased by  $\sim 250$  times (relative error 1%) with single-operator methods. We expect the computation time for solving a 3-D PDM to be at most 250 times slower than the 2-D PDM because of the sparsity structure of the matrices involved. However, the 3-D problem would necessarily consume more computation time than solving a number of 2-D problems equal to the number of grid points for the third dimension. Thus, the 3-D PDM would be at least 30 times slower than the 2-D. Computation time for MC simulations differ by less than a factor of 2 in going from 2 to 3 state variables.

It appears that population density methods will not be generally applicable as a time saving tool until efficient and accurate dimension reduction methods are developed. The fast computation time for our 2-D method suggests that dimension reduction to a system of evolution equations with 2 variables in addition to time might suffice. In any case, the development of good dimension reduction methods is a challenging problem for future research.

### **Acknowledgments**

This work was supported by NSF grant number BNS0090159. We are grateful to Charles Peskin for his advice in general and for his contribution of the operator splitting method. Cheng Ly was supported by the Department of Defense (DoD) Graduate Fellowship (NDSEG). Felix Apfalter was supported in part by the Mexican Science and Technology Council (CONACyT Grant #132245).

### **Appendix A. Numerical methods**

We discretize the rectangular region of the  $g$ - $v$ -plane into  $n_g \times n_v$  identical rectangular bins with dimension  $\Delta g$  by  $\Delta v$ , where the state variables are allowed to be present. When the probability densities are evaluated at points centered in these bins, we obtain a matrix of density values at each point in time. We define a matrix of non-refractory probability density

values  $R(t)$  by  $R_{ij}(t) = \rho(v_i, g_j, t)$ . We denote by  $R_{\bullet j}(t)$  the  $j$ th column of this matrix and by  $R_{i\bullet}(t)$  the  $i$ th row. In a similar manner, we define a matrix of probability density values for the refractory probability density,  $Z(t)$ , where  $Z_{ij}(t) = \sigma(s_i, g_j, t)$ .

Each partial derivative in the divergence of the probability flux vector is approximated by a centered difference quotient, in which fluxes are evaluated at half-grid points.

### Advection operators

Although advective fluxes at half-grid points are approximated by a second-order accurate scheme, the difference between fluxes at two adjacent grid points results in cancellation of the second-order error term. Consequently, the centered difference quotient is a second-order accurate approximation to the partial derivative. For sake of stability of the numerical method, the advective flux at a half-grid point is approximated using the two closest grid points in the positive direction if this flux is negative, or using the two closest grid points in the negative direction if the flux is positive. For example,  $\partial/\partial v \mathcal{F}_v(v_i, g_j, t)$  is approximated by  $[\mathcal{F}_v(v_{i+1/2}, g_j, t) - \mathcal{F}_v(v_{i-1/2}, g_j, t)]/\Delta v$ , where  $v_{i\pm 1/2} = v_i \pm \Delta v/2$ . The approximation for  $\mathcal{F}_v(v_{i\pm 1/2}, g_j, t)$  is determined by first writing (Equation 7) as

$$\mathcal{F}_v(v, g, t) = -\frac{1}{\tilde{\tau}(g)}[v - \tilde{\mathcal{E}}(g)]\rho(v, g, t), \quad (54)$$

where  $\tilde{\mathcal{E}}(g) = (\mathcal{E}_r + g\mathcal{E}_e)/(1 + g)$  is a conductance-dependent target voltage for the advective voltage flux, and  $1/\tilde{\tau}(g) = \frac{1+g}{\tau_m}$  is a time-constant weighted by the excitatory conductance. We use an upwind difference scheme to approximate the flux at half-grid points, *i.e.*,  $\mathcal{F}_v(v_{i+1/2}, g_j, t)$  is approximated by either  $[3\mathcal{F}_v(v_i, g_j, t) - \mathcal{F}_v(v_{i-1}, g_j, t)]/2$ , if  $\tilde{\mathcal{E}}(g_j) > v_{i+1/2}$ , or by  $[3\mathcal{F}_v(v_{i+1}, g_j, t) - \mathcal{F}_v(v_{i+2}, g_j, t)]/2$ , if  $\tilde{\mathcal{E}}(g_j) < v_{i+1/2}$ .

If we define the matrix  $P^v(t)$  as the discretized approximation to  $\mathcal{F}_v(v, g, t)$  at the half-grid voltage points and at the conductance grid points, *i.e.*,

$$P_{ij}^v(t) \equiv \mathcal{F}_v(v_{i+1/2}, g_j, t)$$

then  $P_{\bullet j}^v(t)$  is given by an equation of the form  $P_{\bullet j}^v(t) = Q^v(j) \cdot R_{\bullet j}(t)$ , where  $R(t)$  is the matrix of non-refractory density values, and each  $Q^v(j)$  is a banded matrix with a non-zero diagonal, and 1 band below and/or 1 band above the diagonal. There is a non-zero band both above and below the diagonal of  $Q^v(j)$  when the target voltage (defined above) evaluated at  $g_j$  falls within the voltage domain of  $\rho$ . In particular,  $\mathcal{F}_v(v_{th}, g_j, t)$  the voltage flux at threshold (firing rate) per unit conductance is approximated as

$$\mathcal{F}_v(v_{th}, g_j, t) = P_{n_v j}^v(t) = Q_{n_v}^v(j) \cdot R_{\bullet j}(t), \quad (55)$$

and the firing rate is given by

$$r(t) = \Delta g \sum_j Q_{n_v}^v(j) \cdot R_{\bullet j}(t). \quad (56)$$

If we denote by  $D^v(t)$  the discretized approximation to the partial derivative  $-\partial/\partial v \mathcal{F}_v(v, g, t)$ , then  $D_{\bullet j}^v(t)$  is given by an equation of the form  $D_{\bullet j}^v(t) = A^v(j) \cdot R_{\bullet j}(t)$ , where each  $A^v(j)$  is a banded matrix with a non-zero diagonal, and 2 bands below and/or 2 bands above the diagonal, as illustrated in Figure 13. There are non-zero bands both above and below the diagonal of  $A^v(j)$  when the target voltage (defined above) evaluated at  $g_j$  falls within the voltage domain of  $\rho$ . We refer to each  $A^v(j)$  as a *voltage operator* for short.

The partial derivatives of the advection components of probability fluxes in Equation 9, 13, and 15 are all approximated in a similar manner: if  $D_{i,j}^{g,adv}(t)$  approximates



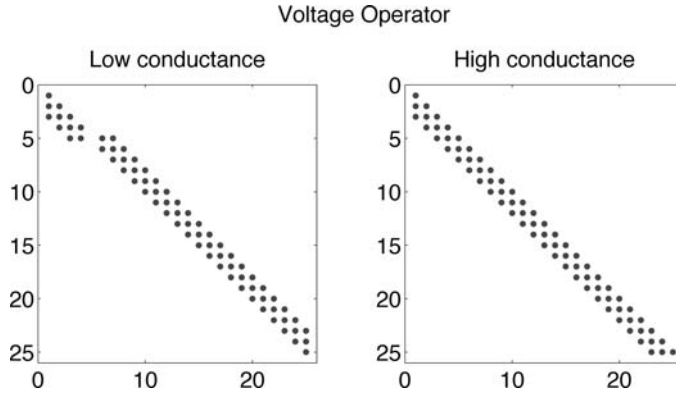


Figure 13. Non-zero elements of voltage operators for low and high conductance values. Voltage operator matrix for a fixed low (left) and a high (right) conductance value. The target voltage is below threshold in the first case and above threshold in the latter. Therefore, the direction of the voltage flux changes at a point in the voltage domain; this is reflected in the operator for a low conductance value. The voltage component of the probability flux is always positive for the high conductance value. We used 25 voltage bins for these example operators.

$-\partial/\partial g \mathcal{J}_g^{adv}(v, g, t)$  at the grid point value  $(v_i, g_j)$  then  $D_{i\bullet}^{g,adv}(t) = R_{i\bullet}(t) \cdot A^{g,adv}$ . Similarly,  $D_{ref}^{g,adv}(t)$  approximates  $-\partial/\partial g \mathcal{J}_{g,ref}^{adv}(s, g, t)$  at grid points and is given by the equation  $(D_{ref}^{g,adv})_{i\bullet}(t) = Z_{i\bullet}(t) \cdot A^{g,adv}$ . We refer to  $A^{g,adv}$  as *advective conductance operator*, and in our case it is a banded matrix with non-zero entries only on the main diagonal and the two bands above it.

If we define the matrix  $P^s(t)$  as the discretized approximation to  $\mathcal{J}_s(s, g, t)$  at the half-grid refractory-time points and at the conductance grid points, i. e.,

$$\mathcal{J}_s(s_{i+1/2}, g_j, t) = P_{ij}^s(t),$$

then  $P_{\bullet j}^s(t)$  is given by an equation of the form  $P_{\bullet j}^s(t) = Q^s \cdot Z_{\bullet j}(t)$ , where  $Z(t)$  is the matrix of refractory density values, and each  $Q^s(j)$  is a banded matrix with a non-zero diagonal, and 1 band below the diagonal (from upwind approximation of the flux at half-grid points). In particular,  $\mathcal{J}_s(\tau_{ref}, g_j, t)$  the refractory-time flux at  $s = \tau_{ref}$  per unit conductance is approximated as

$$\mathcal{J}_s(\tau_{ref}, g_j, t) = P_{n_s j}^s(t) = Q_{n_s \bullet}^s \cdot Z_{\bullet j}(t). \quad (57)$$

Finally, the matrix  $D^s(t)$  that approximates the partial derivative  $-\partial/\partial s \mathcal{J}_s(s, g, t)$  is given by  $D_{\bullet j}^s(t) = A^s \cdot Z_{\bullet j}(t)$ . We call  $A^s$  the *refractory time operator*. As a consequence of upwind differencing, it is a banded matrix with nonzero entries only in the main diagonal and in the two bands below it, as illustrated in Figure 13.

### Excitatory integral operator

The integral components of the probability fluxes  $\mathcal{J}_g^{int}(v, g, t)$  and  $\mathcal{J}_{g,ref}^{int}(s, g, t)$  in Equation 10 and 16 are approximated at half-grid points by quadratic interpolation of the density functions between grid points (Nykamp & Tranchina 2000a), followed by analytic evaluation of the resulting integrals. The quadratic interpolation is based on a truncated Taylor series approximation for the density function at non-grid points, in which the derivatives are approximated by finite differences. This analytic evaluation is straightforward because our particular

probability density function for the integral of the unitary postsynaptic conductance event,  $f_A(x)$ , is represented by a quadratic polynomial over limited domain and zero outside of it. We break up the integral into a sum of integrals over conductance bins, so that we have a maximum number of conductance bins (say  $h$ ) that can contribute to the flux of probability across a half-grid point. When  $D_{ij}^{g,int}(t) = \partial/\partial g \mathcal{J}_g^{int}(v_i, g_j, t)$  is approximated by a centered difference quotient,  $D_{ij}^{g,int}(t)$  is given by an equation of the form  $D_{i\bullet}^{g,int}(t) = R_{i\bullet} \cdot M(t)$ , where the excitatory integral operator  $M(t)$  is banded with one band above the diagonal, a non-zero diagonal and  $h$  bands below. The corresponding flux and partial derivative for the refractory probability density are handled in the same way, so that  $(D_{ref}^{g,int})_{i\bullet}(t) = Z_{i\bullet} \cdot M(t)$ , where the matrix  $M(t)$  is the same for the refractory and non-refractory probability densities.

The advection operator and the excitatory integral operator for conductance can be combined into one operator:  $B(t) = A^{g,adv} + M(t)$ , and we refer to  $B(t)$  as the (total) conductance operator for short.

### System of ODEs for discretized evolution equations

After discretizing the evolution equations for the non-refractory and refractory probability density functions as described above, we obtain

$$\frac{d}{dt} \rho(v_i, g_j, t) = \sum_k A_{ik}^v(j) \rho(v_k, g_j, t) + \sum_n \rho(v_i, g_n, t) B_{nj}(t) + \Phi_{ij}(t), \quad (58)$$

$$\frac{d}{dt} \sigma(s_i, g_j, t) = \sum_k A_{ik}^s \sigma(s_k, g_j, t) + \sum_n \sigma(s_i, g_n, t) B_{nj}(t) + \Psi_{ij}(t), \quad (59)$$

where  $\Phi_{ij}(t)$  is the source of probability density per unit time from the flux of probability out of the refractory pool, and  $\Psi_{ij}(t)$  is a source of probability density per unit time from neurons crossing threshold voltage in the non-refractory pool and then entering the refractory pool.  $\Phi_{ij}(t)$  is equal to zero for all  $i$  except the particular  $i$ ,  $i = i_{reset}$ , corresponding to the voltage bin in which  $v_{reset}$  falls.  $\Psi_{ij}(t) = 0$  for all  $i$  except  $i = 1$ , corresponding to the first refractory time bin (with left edge equal to zero). These source terms are given by

$$\begin{aligned} \Phi_{ij}(t) &= \frac{\delta_{ii_{reset}}}{\Delta v} \mathcal{J}_s(\tau_{ref}, g_j, t) \\ &= \frac{\delta_{ii_{reset}}}{\Delta v} Q_{n_i\bullet}^s \cdot Z_{\bullet j}(t) \\ &= \frac{\delta_{ii_{reset}}}{\Delta v} \sum_m Q_{n_i m}^s \sigma(s_m, g_j, t) \end{aligned} \quad (60)$$

$$\begin{aligned} \Psi_{ij}(t) &= \frac{\delta_{i1}}{\Delta s} \mathcal{J}_v(v_{th}, g_j, t) \\ &= \frac{\delta_{i1}}{\Delta s} Q_{n_v\bullet}^v(j) \cdot R_{\bullet j}(t) \\ &= \frac{\delta_{i1}}{\Delta s} \sum_m \rho(v_m, g_j, t) Q_{n_v m}^v(j) \end{aligned} \quad (61)$$

In the special case where the refractory period  $\tau_{ref} = 0$ ,  $\Phi_{ij}(t) = \frac{\delta_{ii_{reset}}}{\Delta v} \sum_m \rho(v_m, g_j, t) Q_{n_v m}^v(j)$ .

*Single operator method*

The system of equations for the two probability densities Equations 58–61 can be solved by first defining a single density vector  $\vec{\rho}$ , of length  $n_v * (n_g + n_s)$ , that includes all the elements of  $R$  and  $Z$ , and a single matrix operator  $A$ . The first  $n_v * n_g$  elements of  $\vec{\rho}$  are taken from  $R$ , and the remaining  $n_v * n_s$  elements are taken from  $Z$  as follows:

$$\begin{aligned}\vec{\rho}_{(j-1)*n_v+1}(t) &\equiv R_{i,j}(t) && \text{for } j = 1, 2, \dots, (n_g - 1) \text{ and } i = 1, 2, \dots, n_v \\ \vec{\rho}_{n_v*ns+(m-1)*n_v+k}(t) &\equiv Z_{k,m}(t) && \text{for } m = 1, 2, \dots, (n_s - 1) \text{ and } k = 1, 2, \dots, n_v\end{aligned}\quad (62)$$

Now the evolution equation for  $\vec{\rho}$  can be written as

$$\frac{d}{dt}\vec{\rho} = Q(v(t))\vec{\rho}(t), \quad (63)$$

where the elements of  $Q$  are defined by using the definition of  $\vec{\rho}$  above, along with Equations 58–61. In this notation, the firing rate is given by

$$r(t) = \vec{b} \cdot \vec{\rho}(t), \quad (64)$$

where  $\vec{b}$  is a time-independent vector whose elements are determined by Equation 65 and the definition of  $\vec{\rho}(t)$  above.

A straightforward, second-order accurate method for solving Equation 63 is the trapezoidal rule. We discretize time  $t$  into steps of length  $\Delta t$ ; define  $t_k \equiv \Delta t$ ;  $\vec{\rho}^k \equiv \vec{\rho}(t_k)$ ;  $Q^k \equiv Q(v(t_k))$ ; and write

$$\frac{\vec{\rho}^{k+1} - \vec{\rho}^k}{\Delta t} = \frac{1}{2}(Q^{k+1}\vec{\rho}^{k+1} + Q^k\vec{\rho}^k). \quad (65)$$

Solving Equation 65 relies on a synaptic delay, so that at time  $t_k$ , the matrix  $Q^{k+1}$  is known.

The matrix  $Q$  in Equation 65 is sparse, and we used sparse solver algorithms to solve this equation. This method is about 6 times slower than the operator splitting method discussed below.

*Operator splitting method*

The operator splitting method allows us to integrate the evolution equations for the non-refractory and refractory probability density functions in a more efficient manner. Our operator splitting method is analogous to that of Khan & Liu (1998) in a 3-D advection-diffusion problem, but only first-order accurate sub-steps are required for overall second-order accuracy in our 2-D problem. This integration is further facilitated by solving for the two density functions on staggered time grids. To get started the integration of the evolution equations for the two density functions starts at time zero, and a first-order accurate integration over a half time step is performed for the refractory density function. The benefit is that the two evolution equations are uncoupled in the following sense: when a time step is taken to update one of the probability density functions, the source of probability from flux out of the other pool is known at the midpoint of the time step.

The basic idea in the operator splitting method is to split each time step into two half time steps. For example, integration of the non-refractory probability density over a full time step is done as follows. The first half time step of numerical integration involves looping over conductance values (indexed by  $j$ ) and solving for  $R_{\bullet j}(t_{k+1/2})$ , the density at all voltages for each value of conductance. In this half time step the terms involving the conductance operator are fixed at the values given explicitly at the end of the previous time step; the source

term  $\Phi$  is set equal to its value at the end of the half time step,  $\Phi(t_{k+1/2})$ , which is known from integration of the refractory density over the previous staggered time step.  $R_{\bullet j}(t_{k+1/2})$  is computed by the backward Euler method using the conductance-dependent voltage operator  $A^v(j)$ . The second half time step involves looping over voltages and solving for  $R_{i\bullet}(t_{k+1})$ , the density at all conductances for each value of voltage (indexed by  $i$ ). In this half time step the terms involving the voltage operator are fixed at the values given at the end of the previous half time step, and again the source term is given by its value at the end of the previous staggered time step. The same approach is used for integrating the refractory density over a time step.

The operator splitting method described above gives the following two systems of equations for updating the non-refractory probability density by one full time step:

$$\begin{aligned} \frac{\rho(v_i, g_j, t_{k+1/2}) - \rho(v_i, g_j, t_k)}{\Delta t/2} &= \sum_h A_{ih}^v(j) \rho(v_h, g_j, t_{k+1/2}) \\ &+ \sum_n \rho(v_i, g_n, t_k) B_{nj}(t_k) + \Phi_{ij}(t_{k+1/2}), \end{aligned} \quad (66)$$

and

$$\begin{aligned} \frac{\rho(v_i, g_j, t_{k+1}) - \rho(v_i, g_j, t_{k+1/2})}{\Delta t/2} &= \sum_h A_{ih}^v(j) \rho(v_h, g_j, t_{k+1/2}) \\ &+ \sum_n \rho(v_i, g_n, t_{k+1/2}) B_{nj}(t_{k+1/2}) + \Phi_{ij}(t_{k+1/2}). \end{aligned} \quad (67)$$

Adding Equations 66 and 67, and multiplying the resulting equation by  $\frac{1}{2}$ , we obtain

$$\begin{aligned} \frac{\rho(v_i, g_j, t_{k+1}) - \rho(v_i, g_j, t_k)}{\Delta t} &= \sum_h A_{ih}^v(j) \rho(v_h, g_j, t_{k+1/2}) \\ &+ \sum_n \rho(v_i, g_n, t_{k+1/2}) \frac{B_{nj}(t_{k+1/2}) + B_{nj}(t_k)}{2} \\ &+ \Phi_{ij}(t_{k+1/2}). \end{aligned} \quad (68)$$

which indicates that the overall scheme is second order accurate in time.

The computations for the first half-time step in Equation 66 can be written in an economical and convenient form using our matrix notation for discretized  $\rho$ :

$$\frac{R_{\bullet j}(t_{k+1/2}) - R_{\bullet j}(t_k)}{\Delta t/2} = A^v(j) \cdot R_{\bullet j}(t_{k+1/2}) + R(t_k) \cdot B_{\bullet j}(t_k) + \Phi_{\bullet j}(t_{k+1/2}). \quad (69)$$

If we define  $W_{ij}(t_{k+1/2}) \equiv A_{i\bullet}^v(j) \cdot R_{\bullet j}(t_{k+1/2})$ , the computations for the second half-time step in Equation 67 can be written as

$$\frac{R_{i\bullet}(t_{k+1}) - R_{i\bullet}(t_{k+1/2})}{\Delta t/2} = W_{i\bullet}(t_{k+1/2}) + R_{i\bullet}(t_{k+1/2}) \cdot B(t_{k+1/2}) + \Phi_{i\bullet}(t_{k+1/2}),$$

but a more convenient form for time stepping is

$$\frac{R_{i\bullet}^T(t_{k+1}) - R_{i\bullet}^T(t_{k+1/2})}{\Delta t/2} = W_{i\bullet}^T(t_{k+1/2}) + B^T(t_{k+1/2}) \cdot R_{i\bullet}^T(t_{k+1/2}) + \Phi_{i\bullet}^T(t_{k+1/2}), \quad (70)$$

For the refractory density we use the same operator splitting method to obtain the refractory probability density at the next time step.

For the first refractory half-time step we solve:

$$\frac{Z_{\bullet j}(t_{k+1}) - Z_{\bullet j}(t_{k+1/2})}{\Delta t/2} = A^s \cdot Z_{\bullet j}(t_{k+1}) + Z(t_{k+1/2}) \cdot B_{\bullet j}(t_{k+1/2}) + \Psi_{\bullet j}(t_{k+1}), \quad (71)$$

and for the second one

$$\frac{Z_{\bullet i}^T(t_{k+3/2}) - Z_{\bullet i}^T(t_{k+1})}{\Delta t/2} = X_{\bullet i}^T(t_{k+1}) + B^T(t_{k+3/2}) \cdot Z_{\bullet i}^T(t_{k+3/2}) + \Psi_{\bullet i}^T(t_{k+1}), \quad (72)$$

where  $X_{ij}(t_{k+1}) = A_{i\bullet}^s \cdot Z_{\bullet j}(t_{k+1})$ .

Equations 69, 70, 71, and 72 can all be rewritten in the form  $A \cdot \vec{x} = \vec{d}$ , where:  $\vec{x}$  is an unknown density vector;  $A$  is a known matrix; and  $\vec{d}$  is a known vector.

### Eigenvector expansion method

Knight et al. (2000) derived an exact theoretical expression for the response of a non-interacting population of neurons (1-D, integrate-and-fire) to a step change in constant rate of postsynaptic current input events. Their model neurons have a fixed shift in voltage upon receiving a synaptic event. Their theoretical result is in the form of a series, but only a small fraction of the terms are required for accurate numerical results. This was an empirical observation. The method can be generalized in a simple manner to a time-dependent synaptic input rate  $v_e(t)$  by approximating  $v_e(t)$  as piecewise constant. Hence, the eigen method can be a time-saving computational tool because the solution only requires dot-products and sums of a small percentage of the eigenvectors rather than solving a matrix-vector equation at each step. We have successfully applied their method to our formulation of the population density equations with dynamic input, altered the method to allow a refractory period, and extended the method to our 2-D PDM with excitation only. For simplicity, we take  $v_{reset} = \mathcal{E}_r$ .

**2-D excitatory population.** We will first consider our 2-D PDM Equations 6–17. In order to apply the methods of Knight et al. (2000) to our problem with a refractory period, we must concatenate the densities  $\rho(v, t)$  and  $\sigma(s, t)$  and discretize (denoted by  $\vec{\rho}(t)$ ). The result is a linear system (see Equation 63):

$$\frac{d}{dt} \vec{\rho} = Q(v(t)) \vec{\rho}(t).$$

The right hand side of Equation 63 is linear in  $\vec{\rho}(t)$ ;  $Q(v_e(t))$  operates linearly on  $\vec{\rho}(t)$ . This fact is important for applying the eigenvector expansion (see below). If we track the evolution of  $\rho(v, t)$  and  $\sigma(s, t)$  separately instead of using a single operator, the eigenvector theory (Knight et al. 2000) is more complicated and not directly applicable.

Let us consider a step change in steady input rate ( $v_e(t)$ ). Let  $\vec{\rho}_0$  be the density at the previous input rate. We want to solve for  $\vec{\rho}(t)$  for constant input  $v$ . The eigenvalues and eigenvectors of  $Q(v)$  are:

$$Q(v) \vec{\phi}_n = \lambda_n \vec{\phi}_n. \quad (73)$$

The eigenvectors  $\vec{\phi}_n$  are a full set, so  $\vec{\rho}(t)$  can be written in terms of  $\vec{\phi}_n$ . Let  $\vec{\phi}_n^*$  be the eigenvectors of the transpose  $Q(v)^*$ , and recall  $(\vec{\phi}_n^*, \vec{\phi}_n) = \delta_{nn}$ . Substituting

$$\vec{\rho}(t) = \sum_n c_n(t) \vec{\phi}_n$$

into Equation 63 and taking the dot product with  $\vec{\phi}_n^*$  for each  $n$  results in a system of first-order ODEs for  $c_n(t)$ . The vector  $\vec{\rho}_0$  is the concatenated non-refractory and refractory densities at  $t = 0$ . The initial condition

$$\sum_n c_n(0) \vec{\phi}_n = \vec{\rho}_0$$

$$\Rightarrow c_n(0) = (\vec{\phi}_n^*, \vec{\rho}_0)$$

allows us to solve for  $c_n(t)$ . The result is (Knight et al. 2000):

$$\vec{\rho}(t) = \sum_n (\vec{\phi}_n^*, \vec{\rho}_0) e^{\lambda_n t} \vec{\phi}_n. \quad (74)$$

To apply this method to a wider range of inputs  $v_e(t)$ , we precomputed the eigenvectors and eigenvalues of the operator  $Q(v)$  on a grid of  $v$  values. Equation 74 is only valid for constant  $v$ . Our method assumes that  $v_e(t)$  varies smoothly (slowly) enough that it is well approximated by step (piecewise constant) functions. For a time step  $t_k$  to  $t_{k+1}$ , we approximate the input  $v_e(t)$  via  $v = v_e(t_{k+1/2})$ . We assume the densities vary smoothly with  $v$ , and linearly interpolate the density  $\vec{\rho}(t)$ . Let  $\vec{\rho}_1$  and  $\vec{\rho}_2$  be the densities computed via Equation 74 for  $v_1$  and  $v_2$ . For  $v_1 \leq v \leq v_2$ , the density that corresponds to  $v$  is:

$$\vec{\rho} = \vec{\rho}_1 + \frac{v - v_1}{v_2 - v_1} (\vec{\rho}_2 - \vec{\rho}_1). \quad (75)$$

If  $v < v_{\min}$ , then the 2 smallest input values are used to interpolate; similarly for  $v > v_{\max}$ . The smallest  $v$  in our grid corresponds to a very small (almost 0) response. The response is determined by  $\vec{b} \cdot \vec{\rho}$ .

Only a fraction of the terms in Equation 74 are needed in the expansion to obtain good results. Because all  $\lambda_n \leq 0$ , with only  $\lambda_0 = 0$ , we choose the eigenvectors and eigenvalues with the largest  $\lambda_n$  (in the integer sense) because term  $e^{\lambda_n t}$  implies the smallest (largest negative number)  $\lambda_n$ 's decays the quickest. Note that  $\vec{\phi}_0$  is the steady-state solution.

The eigenvectors/values were precomputed for  $1000 \text{ Hz} \leq v \leq 4000 \text{ Hz}$ , on a grid of  $\Delta v = 50 \text{ Hz}$ . Simulations with input from sums of sinusoids with random frequencies and amplitudes are shown in Figure 14. The discretization is as follows: 25 voltage ( $v$ ) bins, 25 conductance bins ( $g$ ), 8 refractory time ( $s$ ) bins, with a time step of 2 ms. For the trapezoidal solver, the time step is 0.25 ms with the same discretization (which gives a relative error of about 2% compared to our finest discretizations). The eigenvector expansion method only uses 10/825 eigenvectors for higher input rates, 25/825 for middle input rates, and 60/825 for lower input rates. The number of eigenvectors was determined by experimentation. Results are shown in Figure 14, the match to the second order accurate trapezoidal rule is good.

**1-D excitatory population.** We now consider a single population of integrate-and-fire neurons that receive excitatory synaptic input:

$$\tau_m \frac{dV}{dt} + (V - \mathcal{E}_r) + G_e(t) \cdot (V - \mathcal{E}_e) = 0 \quad (76)$$

$$G_e(t) = \sum_k A^k \delta(t - T^k), \quad (77)$$

where  $A^k$  is a random size of the magnitude of the delta function,  $T^k$  is a random variable governed by an inhomogeneous Poisson process with mean  $v_e(t)$ . Upon receiving an excitatory



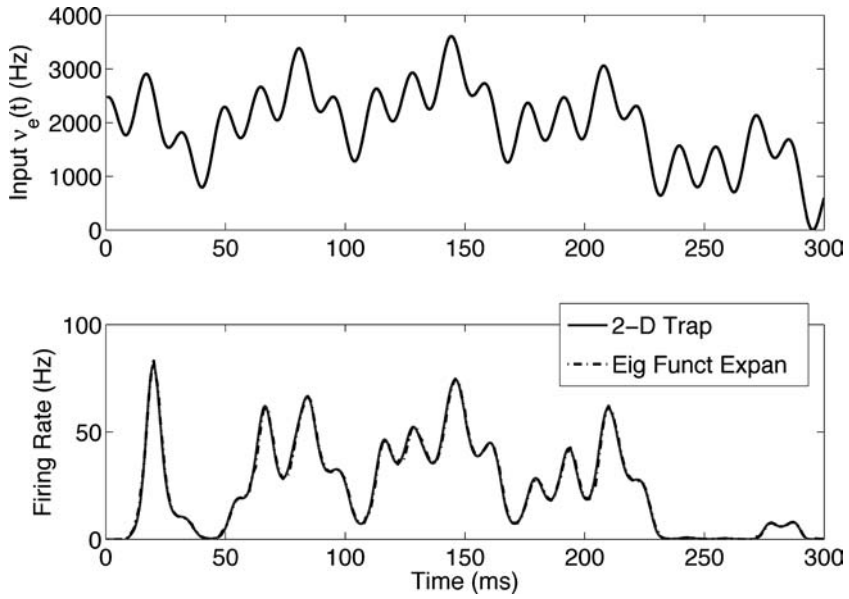


Figure 14. Input and comparison of response of 2-D excitation only problem. The response (lower panel) using the eigenvector expansion method is accurate compared to the standard trapezoidal solver. For trapezoidal rule, we used a time step of 0.25 ms with 25 voltage ( $v$ ) and 25 conductance ( $g$ ) bins, 8 refractory time ( $s$ ) bins to give a total dimension of  $825 \times 825$ . For the eigenvector expansion, we used a time step of 2 ms with 10/825 eigenvectors (in expansion) for higher input rates, 25/825 for middle input rates, 60/825 for lower input rates. Parameters:  $\tau_m = 20$  ms;  $\tau_e = 5$  ms;  $\mathcal{E}_r = -70$  mV;  $v_{th} = -55$  mV;  $\tau_{ref} = 2$  ms;  $\mu_{EPSP} = 0.31$  mV.

conductance event, the neuron's voltage instantaneously jumps from  $V^-$  to  $V^+$  (Nykamp & Tranchina 2000a) via:  $V^+ = V^- + (1 - e^{-\Delta t/\tau_m}) \cdot (\mathcal{E}_e - V^-)$ . Let  $\tilde{F}_{\Gamma^*}$  be the complementary cumulative distribution function of  $\Gamma^* \equiv 1 - e^{-\Delta t/\tau_m}$  (note: this is the same  $\Gamma^*$  in the previous sections). We also include a refractory period  $\tau_{ref}$ .

The population density equations of 76–77 for  $v_{reset} = \mathcal{E}_r \leq v \leq v_{th}$  is:

$$\frac{\partial \rho(v, t)}{\partial t} = -\frac{\partial}{\partial v} \left\{ -\frac{\rho(v, t)(v - \mathcal{E}_r)}{\tau_m} + v_e(t) \int_{\mathcal{E}_r}^v \tilde{F}_{\Gamma^*} \left( \frac{v - v'}{\mathcal{E}_e - v'} \right) \rho(v', t) dv' \right\}. \quad (78)$$

The evolution equation for the refractory density  $\sigma(s, t)$  ( $0 \leq s \leq \tau_{ref}$ ) is:

$$\frac{\partial \sigma(s, t)}{\partial t} = -\frac{\partial \sigma(s, t)}{\partial s}, \quad (79)$$

with boundary conditions:

$$\mathcal{J}_V(v_{th}, t) = \sigma(0, t) \quad (80)$$

$$\sigma(\tau_{ref}, t) = \mathcal{J}_V(\mathcal{E}_r, t), \quad (81)$$

where  $\mathcal{J}_V(v, t) = -\frac{\rho(v, t)(v - \mathcal{E}_r)}{\tau_m} + v_e(t) \int_{\mathcal{E}_r}^v \tilde{F}_{\Gamma^*} \left( \frac{v - v'}{\mathcal{E}_e - v'} \right) \rho(v', t) dv'$ . There is also a zero density boundary condition at threshold voltage:  $\rho(v_{th}, t) = 0$ . The population firing rate is:

$$r(t) = \mathcal{J}_V(v_{th}, t) = v_e(t) \int_{\mathcal{E}_r}^{v_{th}} \tilde{F}_{\Gamma^*} \left( \frac{v_{th} - v'}{\mathcal{E}_e - v'} \right) \rho(v', t) dv'. \quad (82)$$

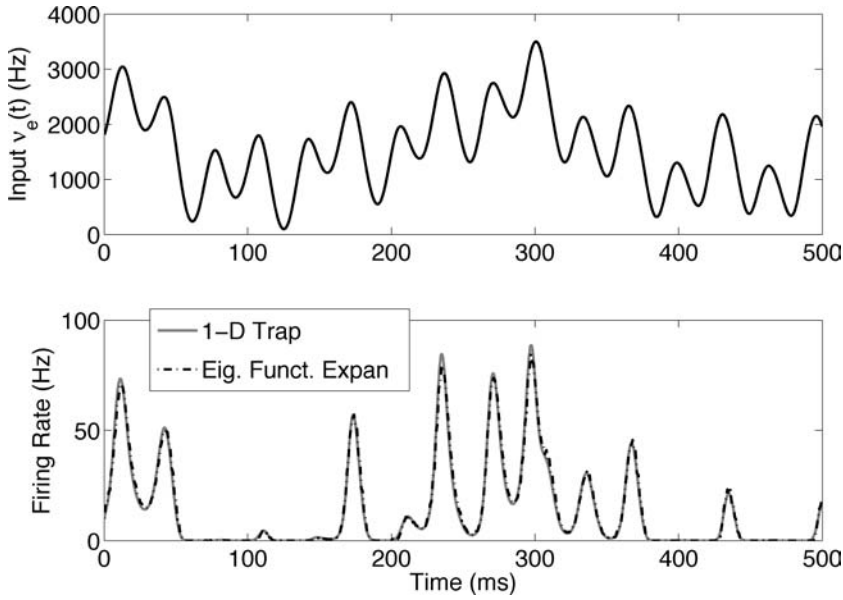


Figure 15. Input and comparison of response of 1-D excitatory population. The response (lower panel) using the eigenvector expansion method is accurate compared to the standard trapezoidal solver. For trapezoidal rule, we used a time step of 0.25 ms with 60 voltage ( $v$ ) bins and 8 refractory time ( $s$ ) bins. For the eigenvector expansion, we used a time step of 2 ms with 3/68 eigenvectors (in expansion) for higher input rates, and 8/68 for lower input rates. Parameters:  $\tau_m = 20$  ms;  $\mathcal{E}_r = -70$  mV;  $v_{th} = -55$  mV;  $\tau_{ref} = 2$  ms;  $\mu_{\Gamma^*} = 7.14 \times 10^{-3}$  so that  $\mu_{EPSP} = 0.5$  mV for  $v^- = \mathcal{E}_r$ .

Naturally, the total densities integrates to 1:

$$\int_{\mathcal{E}_r}^{v_{th}} \rho(v, t) dv + \int_0^{\tau_{ref}} \sigma(s, t) ds = 1.$$

When one concatenates the densities  $\rho(v, t)$  and  $\sigma(s, t)$  and discretize Equations 78–81, the result is similar to the 2-D problem above:

$$\frac{d}{dt} \vec{\rho} = \mathcal{Q}^1(v(t)) \vec{\rho}(t). \quad (83)$$

Recall  $\vec{\rho}(t)$  denotes the discretized functions  $\rho(t)$  and  $\sigma(t)$ . From here, everything follows similarly as in the 2-D case. We exploit the linearity of the right-hand-side of 83 to write out an expansion just like Equation 74 for  $\vec{\rho}(t)$ .

The eigenvectors/values were precomputed for  $800 \text{ Hz} \leq v \leq 4000 \text{ Hz}$ , on a grid of  $\Delta v = 50 \text{ Hz}$ . Simulations with input from sums of sinusoids with random frequencies and amplitudes are shown in Figure 15. The discretization is as follows: 60 voltage ( $v$ ) bins, 8 refractory time ( $s$ ) bins, with a time step of 2 ms. For the trapezoidal solver, the time step is 0.25 ms with the same discretization (which gives a relative error of less than 1% compared to our finest discretizations). The eigenvector expansion method only uses 3/68 eigenvectors for higher input rates, and 8/68 for lower input rates. When the response has a large jump, the eigen-vector method misses the peak of the response. However, for the most part, the method matches well with the second order accurate trapezoidal rule.

*Results and shortcomings with the eigenvector expansion method.* The eigenvector expansion method is faster computationally because unlike with any ordinary finite difference scheme (i.e., trapezoidal rule), we do not have to solve a matrix-vector equation at each time step. Rather, the eigenvector expansion method only requires some dot-products and matrix-vector multiplications. In addition, the method allows one to take bigger time steps (2 ms for Figure 14 and 15), whereas with the trapezoidal solver for the 2-D PDM, the time step must be 0.25 ms or less because Equations 6–17 are stiff. With the 1-D PDM Equation 78–81, the time step for the trapezoidal solver can be larger, but for the sake of consistency we used the same one. The number of eigenvectors required in the expansion is  $\sim 10\%$  or less. For higher synaptic inputs, only 3 out of 68 eigenvectors are required for the 1-D problem, and 10 out of 825 for the 2-D problem. With lower inputs, more eigenvectors are required to capture the response. Remarkably, the inaccuracy of the previous density  $\bar{\rho}_0$  (because it is linearly interpolated) does not effect the accuracy of the response at the next time step. This was true over very long periods of time.

We tried quadratic interpolation to see if some of the jaggedness of the response could be smoothed out, but it was not any better than the linear interpolation. It only increased the computation time.

The eigenvector expansion method has shortcomings. One has to recompute the eigenvectors/values if other parameters change. Also, one has to roughly know the range of inputs ahead of time and experiment with how many eigenvectors are required in the expansion to accurately capture the response. Lastly, the linear interpolation of the density assumes that the input  $v_e(t)$  is almost constant, so if  $v_e(t)$  is rapidly varying, the method requires smaller time steps.

## Appendix B. Parameters

We generally used a membrane time constant  $\tau_m = 20$  ms for all our population density and direct simulations, with the excitatory time constant  $\tau_e = 5$  ms. In the population density method, we chose the time mesh size  $\Delta t$  to be a function of the excitatory time constant,  $\Delta t = \tau_e/tf$ , where  $tf$  is an integer factor. We used  $tf = 10, 20$  and  $40$ , making  $\Delta t = 0.5, 0.25$  and  $0.125$  ms respectively when we tested accuracy and convergence. In the direct Monte-Carlo simulations, on the other hand, we counted firing events to create the Monte-Carlo histograms, and we placed the events in time bins of 2 ms size (the refractory period is  $\tau_{ref} = 3$  ms). Therefore, in order to compare population density methods and direct simulations we integrated the PDM rate over as many  $\Delta t$  intervals as fit into one histogram bin (2 ms) of the Monte-Carlo simulations using the trapezoidal integration rule.

We used the same set of biophysical parameters (reversal potentials, time constants, refractory period and reset voltage) for all the simulations in Sections 4, 5 and 7, except where we explicitly mentioned that we made  $\tau_i$  faster.

The reversal potentials  $\mathcal{E}_e$ ,  $\mathcal{E}_i$  and  $\mathcal{E}_r$  and the voltage threshold  $v_{th}$  had values of 0 mV,  $-70$  mV,  $-65$  mV and  $-55$  mV, respectively, in all the simulations in Sections 4, 5, 7.

The time constants had the values  $\tau_m = 20$  ms,  $\tau_e = 5$  ms;  $\tau_{ref} = 3$  ms in the examples in sections 4, 5, and 7. For the inhibitory time constant we used the values  $\tau_i = 15$  ms and  $\tau_i = 5$  ms as mentioned in the section.

## Appendix C. Distribution of conductance jumps

The conductance jumps were distributed according to a parabolic distribution with mean  $\mu_{A_s}$  (where  $s = e/i$  for excitatory/inhibitory synapses) and support in  $[0, 2\mu_{A_s}]$ , whose density

function is given by

$$f_s(x) = \frac{3}{4\mu_{A_i}^3} x (2\mu_{A_i} - x) \quad (84)$$

We defined

$$\mu_{A_i} = EPSP \frac{\tau_m}{\mathcal{E}_e - \mathcal{E}_r} \quad (85)$$

We chose  $\mu_{A_i}$  to give an *EPSP* amplitude, starting from an initial condition  $v = \mathcal{E}_r$ , of  $\mu_{EPSP} = 0.31$  mV.

We obtain this value by numerically solving the differential equation for the voltage given that the conductance events follow first order kinetics. Solving this equation gives us a voltage waveform in time. We then obtain  $\mu_{EPSP}$  by finding the maximum difference between this waveform and the one obtained from solving equation in the absence of a conductance event. This is explained in more detail below for the case of inhibitory kinetics.

For inhibitory synaptic kinetics, we compute  $\mu_{IPSP}$  in the same way by numerically solving the differential equation

$$\frac{dv}{dt} = -\frac{1}{\tau_m} [(v - \mathcal{E}_r) + G_i(t)(V - \mathcal{E}_i)] \quad (86)$$

starting from the initial condition  $v = \mathcal{E}_r$  and comparing the resulting waveform to the one obtained from

$$\frac{dv}{dt} = -\frac{1}{\tau_m} (v - \mathcal{E}_r) \quad (87)$$

starting at the same initial condition. The value  $\mu_{IPSP}$  is then given by the maximum of the absolute difference between the two waveforms. For completeness, we also indicate the value of  $\mu_{IPSP}^{th}$  that is obtained when the initial condition is  $v = v_{th}$ , which we indicate with a superscript  $th$ .

#### Appendix D. Monte-Carlo simulations

In this section, we describe the numerical methods we use for the Monte-Carlo simulations in the excitation only case. When adding inhibition, the method is similar, so we only discuss the case where all the synapses are excitatory.

The state of every non-refractory integrate-and-fire point neuron in a population is described by its voltage  $V(t)$  and conductance  $G_e(t)$ ; the evolution of these state variables is given in Equations 2 and 3. We use a second-order accurate integration scheme in time, the trapezoidal rule, to integrate  $V$  and  $G_e$  between postsynaptic conductance events.

To generate the synaptic conductance events from external input to each neuron during each time step, we draw a random number of excitatory conductance external events  $N_e$  from a Poisson distribution with expected number  $\bar{N}_e = \nu_e(t_k)\Delta t$ , where  $\nu_e(t_k)$  is the rate of external synaptic events. The arrival time for each generated event within the interval is chosen independently from a uniform distribution. If the neurons receive internal events from neurons in other populations (or from the same population), then we add these event times to our list of external event times and we sort the vectors of total (external and internal) event times (with inhibition, we would have to consider whether the events are excitatory or inhibitory as well). Then, instead of generating the magnitude of the conductance events and updating the voltage and conductance of the neurons between events neuron by neuron (as in Haskell (2000)), we loop over the total number of events per neuron and update the

voltage, conductance and synaptic jump values in a vectorized manner. We update a large number of neurons in a block by grouping them up according to their number of events. If in a given time step the maximal number of total events is  $n_{\max}$ , then we consider in the first step in the internal loop the first event interval of the neurons with  $n_{\max}$  events, in the second step of the internal loop, the first event interval of the neurons with one less events and the second event interval of the neurons with  $n_{\max}$  events; in the third step of the loop, the first event of the neurons with  $n_{\max} - 2$  events, the second event of the ones with  $n_{\max} - 1$  events and the third event interval of the ones with  $n_{\max}$  events. Continuing in this fashion, at the last step we consider the neurons with no events at all (the time interval is then  $\Delta t$ ), together with all other neurons whose last event was some time in the interval of width  $\Delta t$ . At the “plus side” of each event time the synaptic input jumps by  $A_e/\tau_e$ . The voltage and conductance evolve continuously between events.

At every step in the internal loop, we group the neurons to be considered in that loop into categories: the ones that are to be integrated in that step of the internal loop and were non-refractory at the start of the time interval and the ones that are coming out of the refractory period in the given time interval. The conductances of all neurons decay exponentially in all the intervals between event times (or for the whole time step  $\Delta t$  in the absence of event times). We update the conductance of all neurons that are considered in the given step of the internal loop first. Then the voltage of the neurons that are in their non-refractory period is updated. For the neurons for which the membrane potential crosses the threshold voltage, we record the firing time, increase the counter of firing neurons in the time step, reset the voltage and put the respective neurons in the refractory pool in a waiting queue of duration  $\tau_{\text{ref}}$ , where only their conductances get updated. If voltage crosses threshold in some time step, then the time of crossing is determined with second order accuracy. If there is connectivity and/or multiple populations, we have to keep track of the connectivity of the neurons that just fired and set-up in a queue matrix the internal events resulting from the firing of the neurons in presynaptic populations and connecting to postsynaptic neurons in the same or other populations. We also keep track of different (random) synaptic latencies which affect the order of arrival of events into the postsynaptic neurons. Synaptic failure, when included, randomly causes the cancellation of some internal synaptic events. In our model there is a maximal latency for synaptic transmission. Consequently, any synaptic event generated by a spike in the interval  $(t_k, t_{k+1})$  will have an effect at a future time before time  $t_{k+1+m}$ , where  $m\Delta t$  is the maximum latency. Thus, internally generated events can be stored in an array in which future arrival times are stored in  $m$  time bins. Including the time bin in which the spike occurred (*i.e.*, the current integration time) gives  $m + 1$  time bins in total for the queue matrix. After a full time step  $\Delta t$  is over, the first time bin is discarded, a pointer moves over by one time bin, and another time bin is added onto the end of the remaining  $m$  time bins. We update the conductances of all neurons that have events in the given step in the event loop by adding a random conductance jump of size  $\frac{A_e}{\tau_e}$  to each one of these neurons at their respective times in a vectorized manner. In this work,  $A_e$  is randomly drawn from a parabolic distribution. Finally, the remaining and elapsed time in the interval is updated for the integration at the next event interval and the internal loop recycles until all events in the time interval  $(t_k, t_{k+1})$  are considered. In this way we obtain the voltage and conductance of every neuron at the next time point.

In the single population case with no connectivity which we treat first, we present the firing rate obtained from the Monte-Carlo methods with either 1000, 10,000 or 100,000 neurons in population. In the examples with multiple populations that we present later, we usually use 100 or 1000 neurons per population and we average the firing rates that we obtain over several realizations. For each realization the detailed connectivity between the neurons in the

different populations is chosen randomly, while keeping the average connectivity between populations fixed at the specified values. The synaptic delays between presynaptic and postsynaptic populations, the magnitude of the conductance jumps and the external Poisson input into the neurons in each population are chosen at random and independently in each realization.

## Appendix E. Full mean-field approximation

The mean-field simulations, as explained in Haskell (2000), are calculated by taking the expected value of the synaptic conductance (Equation 3) over realizations assuming that the input is Poisson. The resulting ODE for the mean synaptic conductance is

$$\tau_e \frac{d}{dt} \mu_{G_e}(t) + \mu_{G_e}(t) = \mu_{A_e} v_e(t). \quad (88)$$

This mean conductance is used in place of the stochastic conductance in the evolution equation for the voltage (Equation 2):

$$\tau_m \frac{dV}{dt} + (V - \mathcal{E}_r) + \mu_{G_e}(t)(V - \mathcal{E}_e) = 0. \quad (89)$$

to calculate (deterministically) the firing rate by integrating this last equation from  $v_{reset}$  to  $v_{th}$ :

$$f_{MF}(t) = \frac{1}{\log \left( \frac{\mathcal{E}(\mu_{G_e}(t) - v_{reset})}{\mathcal{E}(\mu_{G_e}(t) - v_{th})} \right) + \tau_{ref}} \quad (90)$$

where  $\mathcal{E}(g) = \frac{\mathcal{E}_r + g \mathcal{E}_e}{1 + g}$  and where  $f_{MF}$  is zero when the argument of the logarithm is negative.

The average time between spikes in the absence of a refractory period is determined at each time point in time in this approximation by holding the mean conductance fixed at its value at that time and then computing how long it takes for the voltage to evolve from  $v_{reset}$  to  $v_{th}$ . This involves integrating a simple first order ordinary differential equation with constant coefficients (Equation 89 with  $\mu_{G_e}$  fixed). In this case, the firing rate is given by  $\frac{1}{T}$ . When a refractory period  $\tau_{ref}$  is included, the firing rate is given by  $\frac{1}{T + \tau_{ref}}$ .

## References

- Abbott LF, van Vreeswijk C. 1993. Asynchronous states in networks of pulse-coupled oscillators. *Physical Rev E* 48:1483–1490.
- Amit D, Brunel N. 1997. Model of global spontaneous activity and local structured activity during delay periods in the cerebral cortex. *Cerebral Cortex* 7:237–252.
- Brown E, Moehlis J, Holmes P. 2004. On the phase reduction and response dynamics of neural oscillator populations. *Neural Comput* 16:673–715.
- Brunel N. 2000. Dynamics of sparsely connected networks of excitatory and inhibitory spiking neurons. *Journal of Computational Neurosci* 8:183–208.
- Brunel N, Chance F, Fourcaud N, Abbott L. 2001. Effects of synaptic noise and filtering on the frequency response of spiking neurons. *Physical Rev Letters* 8:2186–2189.
- Brunel N, Hakim V. 1999. Fast global oscillations in networks of integrate-and-fire neurons with low firing rates. *Neural Computat* 11:1621–1671.
- Cai D, Tao L, Rangan A, McLaughlin D. 2006. Maximum-entropy closures for kinetic theories of neuronal network dynamics. *Communications in Mathematical Sciences* 4:97–127.
- Cai D, Tao L, Shelley M, McLaughlin D. 2004. An effective kinetic representation of fluctuation-driven neuronal networks with application to simple and complex cells in visual cortex. *Proc Nat Acad Science* 101:7757–7762.



- Casti AR, Omurtag A, Sornborger A, Kaplan E, Knight B, Sirovich L, Victor J. 2002. A population study of integrate-and-fire-or-burst neurons. *Neural Comput* 14:957–986.
- Câteau H, Reyes A. 2006. Relation between single neuron and population spiking statistics and effects on network activity. *Physical Rev Letters* 96:058101.
- Chapman SI, Cowling T. 1970. The mathematical theory of non-uniform gases. New York: Cambridge University Press.
- Doiron B, Rinzel J, Reyes A. 2006. Stochastic synchronization in finite size spiking networks. *Physical Rev E* 74:030903.
- Edmonds B, Gibb AJ, Colquhoun D. 1995. Mechanisms of activation of glutamate receptors and the time course of excitatory synaptic currents. *Annual Rev Physiol* 57:495–519.
- Fain GL. 1999. Molecular and cellular physiology of neurons, chapter 9–11. Cambridge, MA: Harvard University Press.
- Fourcaud N, Brunel N. 2002. Dynamics of the firing probability of noisy integrate-and-fire neuron. *Neural Comput* 14:2057–2110.
- Gerstner W. 1995. Time structure of the activity in neural network models. *Physical Rev E* 51:738–758.
- Gerstner W. 1999. Population dynamics of spiking neurons: Fast transients, asynchronous states, and locking. *Neural Comput* 12:43–90.
- Haskell E. 2000. Population density methods for large-scale modeling of neural networks with realistic synaptic kinetics. PhD thesis, New York University.
- Haskell E, Nykamp DQ, Tranchina D. 2001. Population density methods for large-scale modeling of neuronal networks with realistic synaptic kinetics: Cutting the dimension down to size. *Network: Comput in Neural Systems* 12:141–174.
- Huertas MA, Smith GD. 2006. A multivariate population density model of the dLGN/PN relay. *J Comput Neurosci* DOI: 10.1007/s10827-006-7753-2.
- Khan LA, Liu P-F. 1998. An Operator splitting algorithm for the three-dimensional advection-diffusion equation. *Int J Numerical Methods in Fluids* 28:461–476.
- Knight B, Omurtag A, Sirovich L. 2000. The approach of a neuron population firing rate to a new equilibrium: An exact theoretical result. *Neural Comput* 12:1045–1055.
- Knight BW. 1972a. Dynamics of encoding in a population of neurons. *J General Physiol* 59:734–766.
- Knight BW. 1972b. The relationship between the firing rate of a single neuron and the level of activity in a population of neurons. Experimental evidence for resonant enhancement in the population response. *J General Physiol* 59:767–778.
- Knight BW. 2000. Dynamics of encoding in neuron populations: Some general mathematical features. *Neural Comput* 12:473–518.
- Knight BW, Manin D, Sirovich L. 1996. Dynamical models of interacting neuron populations. In Gerf EC, editor, *Symposium on robotics and cybernetics: Computational engineering in systems applications*, Lille, France: Cite Scientifique.
- Koch C. 1999. Biophysics of computation: information processing in single neurons, chapter 4. New York: Oxford University Press.
- Krukowski AE, Miller KD. 2001. Thalamocortical nmda conductances and intracortical inhibition can explain cortical temporal tuning. *Nature Neurosci* 4:424–430.
- Kuramoto Y. 1991. Collective synchronization of pulse-coupled oscillators and excitable units. *Physica D* 50: 15–30.
- Ly C, Tranchina D. 2006. Critical analysis of dimension reduction by a moment closure method in a population density approach to neural network modeling. *Neural Comput* (in press).
- Mattia M, Giudice PD. 2002. Population dynamics of interacting spiking neurons. *Physical Review E* 66:1–19.
- Moreno-Bote R, Parga N. 2004. Role of synaptic filtering on the firing response of simple model neurons. *Physical Rev Letters* 92:028102.
- Moreno-Bote R, Parga N. 2005. Membrane potential and response properties of populations of cortical neurons in the high conductance state. *Physical Review Letters* 94:088103.
- Nykamp DQ. 2000. A population density approach that facilitates large-scale modeling of neural networks. PhD thesis, New York University.
- Nykamp DQ, Tranchina D. 2000a. A population density approach that facilitates large-scale modeling of neural networks: Analysis and an application to orientation tuning. *J Comput Neurosci* 8:19–50.
- Nykamp DQ, Tranchina D. 2000b. A population density approach that facilitates large-scale modeling of neural networks: Extension to slow inhibitory synapses. *Neural Computation* 13:511–546.
- Omurtag A, Knight BW, Sirovich L. 2000. On the simulation of large populations of neurons. *J Computat Neurosci* 8:51–63.

- Rauch A, Camera GL, Lüscher H, Senn W, Fusi S. 2003. Neocortical pyramidal cells respond as integrate-and-fire neurons to in vivo-like currents. *J Neurophysiol* 90:1598–1612.
- Silberberg G, Wu C, Markram H. 2004. Synaptic dynamics control the timing of neuronal excitation in the activated neocortical microcircuit. *J Physiol* 556:19–27.
- Sirovich L. 2003. Dynamics of neuronal populations: eigenfunction theory; some solvable cases. *Network: Comput Neural Systems* 14:249–272.
- Sirovich L, Knight B, Omurtag A. 2000. Dynamics of neuronal populations: The equilibrium solution. SIAM.
- Treves A. 1993. Mean-field analysis of neuronal spike dynamics. *Network: Comput Neural Systems* 4:259–284.
- Tuckwell HC. 1988a. Introduction to theoretical neurobiology: volume 1, linear cable theory and dendritic structure, chapter 3. New York: Cambridge University Press.
- Tuckwell HC. 1988b. Introduction to theoretical neurobiology: volume 1, linear cable theory and dendritic structure nonlinear and stochastic theories, chapter 9. New York: Cambridge University Press.
- Wang XJ. 1999. Synaptic basis of cortical persistent activity: The importance of NMDA receptors to working memory. *J Neurosci* 19:9587–603.
- Whittington MA, Traub R, Kopell N, Ermentrout B, Buhl EH. 2000. Inhibition-based rhythms: Experimental and mathematical observations on network dynamics. *Int J Psychophysiol* 38:315–336.
- Wilbur W, Rinzel J. 1983. A theoretical basis for large coefficient of variation and bimodality in neuronal interspike interval distributions. *J Theor Biol* 105:345–368.